Prepared for *JPCA*
June 5, 2019

Anharmonic Rovibrational Partition Functions at High Temperatures: Tests of Reduced-Dimensional Models for Systems with up to Three Fluxional Modes

Ahren W. Jasper,[a,*] Lawrence B. Harding,[a] Christopher Knight,[b] and Yuri Georgievskii[a]

[a]*Chemical Sciences and Engineering Division, Argonne National Laboratory, Lemont, IL 60439*

[b]*Computational Sciences Division, Argonne National Laboratory, Lemont, IL 60439*

Abstract. Curvilinear-coordinate Monte Carlo phase space integration and a series of full-dimensional fitted potential energy surfaces are used to study the effectiveness of reduced-dimensional models for predicting rovibrational anharmonicity at high temperatures. Fully coupled and fully anharmonic, but classical, rovibrational partition functions Q are computed for fourteen species with two or three fluxional modes (inversions or torsions) and as many as thirty degrees of freedom. These results are converted to semiclassical anharmonicity correction factors f and are analyzed alongside results obtained previously for twenty-two species with up to two fluxional modes. As expected, fluxional species show considerable variation in f at high temperatures; f is as small as 0.2 for acetone and is as large as 9 for methylene glycol at 2500 K. This set of full-dimensional results is used to test the accuracy of reduced-dimensional models where fluxional modes are treated as coupled to one another but as separable from the remaining nonfluxional modes. For most systems, we find that such an approximation is accurate at high temperatures, with average errors in Q of just ~25%. For some systems, however, larger errors are found, and these are attributed to strong coupling of the fluxional modes to one or more nonfluxional modes. In particular, we identify strong coupling to low-frequency bends for some systems, and we show that by comparing curvilinear and rectilinear harmonic frequencies for the fluxional modes we can estimate the effect of this coupling on rovibrational anharmonicity. We also quantify the accuracy of the more severe but common assumption of treating fluxional modes as separable from one another, i.e., as sets of uncoupled one-dimensional inversions and torsions. This approach can work well for methyl and alkyl rotors, but it is shown to have errors as large as a factor of seven at high temperatures for more complex systems. Finally, we note that while the present analysis focuses on the treatment of fluxional modes, the collective anharmonicity correction associated with the more numerous nonfluxional modes, while simpler to describe, comprises a significant fraction of the overall anharmonicity.

*E-mail: ajasper@anl.gov

1. Introduction

The a priori accuracy of gas phase theoretical rate constants and thermochemistry continues to improve and, in many cases, now rivals that of the best measurements.[1,2] These improvements may largely be attributed to advances in electronic structure theory, which have reduced the errors associated with threshold energies, frequencies, and rotational constants. When high-level electronic structure theory methods are used, the leading remaining sources of error often include the treatment of rovibrational anharmonicity.

Rovibrational anharmonicity corrections include both changes to the zero point energy as well as deviations from uncoupled harmonic vibrational level progressions. The former effect alters the threshold energy (i.e., the barrier height or reaction energy) and thus introduces an error that is largest at low temperatures. Here we consider the error associated with the latter effect, which, in contrast, is exactly zero at the threshold energy and 0 K but increases with energy and can be quite large at high temperatures.

A variety of theoretical methods have been advanced for characterizing rovibrational anharmonicity, including diffusion Monte Carlo,[3,4] variational approaches,[5–16] path integrals,[17–24] direct product diagonalization,[25–35] empirical methods,[36,37] perturbation theories,[38–47] specialized methods for torsions,[48–58] and other separable approaches.[59–62] Many of these methods are designed for spectroscopic applications and are most reliably applied to predict high-accuracy zero point energies and fundamental transition energies. There has been relatively less work done to characterize anharmonicity at high temperatures and energies.

Here we use Monte Carlo phase space integration[63–71] (MCPSI) to compute fully anharmonic and fully coupled, but classical, rovibrational partition functions. These are used to determine rovibrational Pitzer–Gwinn[48] anharmonicity corrections f, which is one of several semiclassical strategies[72–78] that have been developed for improving MCPSI predictions. MCPSI is well-suited for studying rovibrational anharmonicity at high energies and temperatures, as it describes the classical limit without approximation.

We focus on the treatment of fluxional systems, i.e., systems with low-barrier inversions, torsions, or both. Fluxional systems are poorly described as collections of harmonic oscillators. They may have multiple minima, weakly hindered internal

rotations, squarer-than-quadratic inversions, etc., each of which can contribute large positive or negative anharmonicities. The overall anharmonicity is generally difficult to anticipate as it results from the partial cancellation of a variety of positive and negative effects. This is particularly true at high energies and temperatures where the anharmonicity of nonfluxional modes cannot be safely neglected, and the overall anharmonicity may therefore depend strongly on a large number of rovibrational modes and their coupling.

The looseness of fluxional modes presents a challenge to MCPSI sampling. We recently demonstrated the utility of a curvilinear coordinate implementation of MCPSI, and rovibrational anharmonicity corrections f were computed for twenty-two systems with zero, one, or two fluxional modes and as many as eight atoms.[79] Here we consider fourteen more systems with challenging vibrational structures, with two or three fluxional modes, and with as many as eleven atoms. The full set of thirty-six systems is used to study trends in rovibrational anharmonicity as a function of system size and for different types of fluxional modes. The full-dimensional semiclassical MCPSI results are also used as benchmarks to quantify the accuracy of simple reduced-dimensional descriptions of fluxional modes.

This paper is organized as follows. In Sec. 2.1, the full-dimensional rovibrational anharmonicity correction to the partition function, f, and its relationship to the per-mode anharmonicity correction Γ are defined. A reduced-dimensional approach for describing the impact of fluxional modes on f is described in Sec. 2.2, along with variations in its implementation that will be tested throughout Sec. 3. Sections 2.3 and 2.4 briefly provide details related to high performance computing and to the potential energy surfaces used here, respectively. Throughout Secs. 3.1, 3.2, and 3.3, per-mode anharmonicities Γ are presented for each of the thirty-six systems, and various reduced-dimensional models are tested for the thirty-one systems with fluxional modes. A summary of the results of these tests is collected in Table 1. Section 3.4 and Table 4 present an alternate summary of these same results focused on quantifying errors in the total rovibrational anharmonicity correction f, with the goal of providing useful error estimates for reduced-dimensional approaches for modeling rovibrational anharmonicity at elevated temperatures.

2. Theory

2.1. Curvilinear coordinate Monte Carlo phase space integration

Our implementation[70] of curvilinear coordinate MCPSI was recently adapted for treating fluxional species.[79] The result of an MCPSI calculation is the total classical rovibrational partition Q, which is the fully-coupled and fully-anharmonic partition function for all vibrations and rotations. This in turn may be used to define a rovibrational anharmonicity correction factor

$$f \equiv \tfrac{1}{\sigma} Q / Q_{\mathrm{HO}} Q_{\mathrm{RR}} , \tag{1}$$

where σ is the number of classically distinguishable lowest-energy minima, and Q_{HO} and Q_{RR} are harmonic oscillator and rigid rotor partition functions, respectively. The partition functions in eq 1 are all evaluated classically, with Q_{HO} and Q_{RR} calculated analytically using harmonic frequencies and geometries for the lowest-energy local minimum.

The exact (fully-coupled, fully-anharmonic, *and* quantum mechanical) total rovibrational partition function $\tilde{Q}$ can be approximated using f and Pitzer and Gwinn's[48] "useful approximation,"

$$\tilde{Q} \approx f \tilde{Q}_{\mathrm{RR}} \tilde{Q}_{\mathrm{HO}} , \tag{2}$$

where the tilde distinguishes quantum mechanical partition functions from classical ones. Although not motivated in this way by Pitzer and Gwinn in 1942, the above expression can be derived as an approximation to the path integral formulation of $\tilde{Q}$,[80,81] which is an exact quantum mechanical theory, by assuming that the forces governing the imaginary-time paths are harmonic with geometry-independent frequencies corresponding to those used in the expression for $\tilde{Q}_{\mathrm{HO}}$. This idea is central to several semiclassical corrections that have been developed for improving Q.[73–75]

Anharmonicity corrections to the partition function arising from changes to the zero point energy (which can be significant[3,4]) are not accounted for in f. Instead, $f \to 1$ as the temperature $T \to 0$ by construction, and f is therefore the finite-temperature anharmonicity correction or, equivalently, the semiclassical Pitzer–Gwinn approximation to the error in the RRHO partition function with its reference energy set to its zero point energy.

It is useful to consider both the total anharmonicity correction factor f and the

average anharmonicity correction per mode Γ. These quantities are related via

$$f = [1 + \Gamma(T)]^{\alpha-3/2} \quad (3)$$

$$\approx [1 + \Gamma' \, T/T']^{\alpha-3/2} \quad (4)$$

where α is the number of rotational and vibrational degrees of freedom, and overall rotations (of which there are always three for the systems considered here) contribute fractional powers while vibrational modes contribute whole powers. In eq 3, the temperature dependence of $\Gamma(T)$ is explicitly indicated, while in eq 4 just the linear-in-T term has been retained. The coefficient Γ' in eq 4 is independent of temperature, and T' is a reference temperature, which we set to 1000 K.

Equation 4 is a good approximation to eq 3 for nonfluxional species[79] and often for nonfluxional modes in fluxional species, as demonstrated below. When eq 4 is an appropriate representation of eq 3 and with T' = 1000 K, Γ' has the useful interpretation as the average anharmonicity correction to the total partition function per vibrational mode and per 1000 K. The temperature-dependence of the anharmonicity correction associated with the three modes for overall rotational is more complex, but, notably, we typically find that both types of anharmonicity can be usefully characterized via a single shared parameter Γ when f and Γ are related as in eq 3.

Here we report f and Γ for fourteen species with up to three fluxional modes, and these new results are analyzed alongside values of f obtained previously[79] for twenty-two species with zero, one, or two fluxional modes. These thirty-six species are considered in groups labeled (N_t,N_i) based on their numbers of torsions N_t and inversions N_i.

As reported in Ref. 79, very similar values of Γ are obtained for all of the members of the nonfluxional (N_t,N_i) = (0,0) group. This useful result allows us to empirically interpret the average value of Γ for the (0,0) group (which we label $\Gamma_{(0,0)}$ and quantify in Sec. 3.1) as representative of nonfluxional species generally. The anharmonic effects of fluxional modes on Q can be quantified by comparing this standard value for nonfluxional species, $\Gamma_{(0,0)}$, with Γ computed for the fluxional species comprising the (N_t,N_i) = (0,1), (1,0), (1,1), (2,0), (2,1), (1,2), and (3,0) groups. As expected and as detailed throughout Sec. 3, the average values of Γ for the fluxional groups differ significantly from $\Gamma_{(0,0)}$.

2.2. Reduced-dimensional models for fluxional modes

A major goal of this work is to test the accuracy of reduced-dimensional models for describing the anharmonic effects of fluxional torsions and inversions. The reduced-dimensional approaches tested all involve the β-dimensional (βD) fluxional mode partition function

$$q^{\beta\mathrm{D}} = \prod_{i=1}^{\beta} \sqrt{\frac{k_\mathrm{B}T}{\pi A_i}} \int d\varphi_1 \cdots d\varphi_\beta \exp[-V_\beta(\varphi_1,\cdots,\varphi_\beta)/k_\mathrm{B}T], \tag{5}$$

where β is the number of fluxional modes included in the correction, φ_i is the angular coordinate for fluxional mode i, A_i is its effective internal rotational/inversion constant, and V_β is a partially-relaxed β-dimensional potential energy surface, where all of the modes not included in V_β (i.e., all of the nonfluxional modes) have been optimized. The βD model in eq 5 includes full potential coupling between fluxional modes, while the potential coupling between the fluxional and nonfluxional modes is treated adiabatically via the partial optimizations in V_β. No kinetic coupling to or among the fluxional modes is included in eq 5 as the geometry dependence of A_i has been ignored.

For torsions, φ_i is the dihedral angle and A_i is evaluated as the reduced moment of inertia of the two rotating fragments at their equilibrium geometries about their connecting bond, as usual.[48] For bends and inversions, an analogous approach is taken, where A_i is evaluated for infinitesimal changes to the angular coordinate with the rest of the internal coordinates fixed at their equilibrium geometries. For inversions, φ_i is defined as the trisector angle,[82] i.e., the angle that any of the three participating bonds makes with respect to a vector through the central atom defined such that all three angles are equal.

Equation 5 is used to define a β-dimensional fluxional mode correction factor analogous to eq 1,

$$f^{\beta\mathrm{D}} = q^{\beta\mathrm{D}}/q_{\mathrm{HO}*}, \tag{6}$$

where $q_{\mathrm{HO}*}$ is the product of β one-dimensional classical harmonic oscillator partition functions; these are evaluated using frequencies ω_i* obtained by diagonalizing the curvilinear-coordinate hessian of the reduced-dimensional potential V_β and using the

effective masses defined by A_i. With this set of choices, the correction factor $f^{\beta D}$ in eq 6 is independent of A_i, and $f^{\beta D} \to 1$ as $T \to 0$.

With the β fluxional modes described by $q^{\beta D}$, the average per-mode anharmonicity correction $\Gamma^{\beta D}$ for the remaining nonfluxional modes is computed

$$f / f^{\beta D} = [1 + \Gamma^{\beta D}(T)]^{\alpha - \beta - \frac{3}{2}} \tag{7}$$

$$= [1 + \Gamma'^{\beta D} T / T']^{\alpha - \beta - \frac{3}{2}} \ . \tag{8}$$

We find that for some systems $\Gamma^{\beta D}$ shows a linear dependence on T and has a magnitude very close to $\Gamma_{(0,0)}$. We interpret the deviation of $\Gamma^{\beta D}$ from $\Gamma_{(0,0)}$ as a measure of the per-mode error in the reduced-dimensional model in eq 5. Implicit in this analysis is the assumption that $\Gamma_{(0,0)}$ represents not only the average per-mode anharmonicity correction in nonfluxional species, but that $\Gamma_{(0,0)}$ also represents the average per-mode anharmonicity correction of nonfluxional modes in fluxional species. As demonstrated throughout Sec. 3, this assumption appears, at least empirically, to be a useful one. For example, for several systems with relatively large deviations of $\Gamma^{\beta D}$ from $\Gamma_{(0,0)}$, we consider various improvements to the $q^{\beta D}$ model and show that these improvements generally lead to closer agreement of $\Gamma^{\beta D}$ and $\Gamma_{(0,0)}$. While more direct tests of these methods would certainly be desirable, high-accuracy calculations of partition functions for systems with complex rovibrational structures at high energies and temperatures are likely to remain difficult to obtain for some time. The present empirical approach thus provides some means of quantifying errors, or at least sensitivities, in reduced-dimensional approaches, such as the simple ones considered here.

Throughout the analyses presented in Sec. 3, several improvements to the reduced-dimensional model described by eqs 5 and 6 are tested. In one such test, the neglect of kinetic coupling and of coupling to external (overall) rotation in eq 5 is addressed via an implementation of eq 5 where the geometry dependence of A_i due to fluxional motion is incorporated. The analogous modification to Q_{RR} via the fluxional-mode geometry dependence of the overall rotational constants, which we refer to collectively as B_i, is also tested.

We also test a modification to the reduced-dimensional anharmonicity correction

factor $f^{\beta D}$ that approximately accounts for any missing coupling between fluxional and nonfluxional modes while retaining much of the simplicity of the approach. Specifically, we compute

$$\hat{f} = \tilde{q}_{\mathrm{HO}*} / \tilde{q}_{\mathrm{HO}}, \tag{9}$$

where $\tilde{q}_{\mathrm{HO}*}$ and $\tilde{q}_{\mathrm{HO}}$ are the quantum mechanical harmonic oscillator partition functions for the β fluxional modes evaluated using reduced-dimensional curvilinear-coordinate frequencies ω_i* and the usual Cartesian normal mode frequencies ω_i, respectively. When $\omega_i^* \approx \omega_i$, the anharmonic character of the fluxional modes is localized to the motions included in the reduced-dimensional potential V_β, and the correction described by eq 9 is small ($\hat{f} \approx 1$). In contrast, when $\omega_i^* \neq \omega_i$ and $\hat{f}$ deviates significantly from unity, the magnitude of this deviation is one measure of the coupling of the fluxional modes to one or more nonfluxional modes.

As demonstrated below, when this "fluxional mode projection" correction factor $\hat{f}$ deviates from unity by less than ~10%, it is found to be useful as a quantitative correction to $f^{\beta D}$. We test such a model where $\hat{f}^{\beta D} = \hat{f} f^{\beta D}$, and per-mode anharmonicity corrections for the nonfluxional modes, $\hat{\Gamma}^{\beta D}$, are defined as in eqs 7 and 8. When $\hat{f}$ deviates more significantly from unity, $\hat{f}$ is no longer useful as a quantitative correction but is instead diagnostic of significant coupling to one or more nonfluxional modes, such as low-frequency bending motions. When this is the case, improved reduced-dimensional descriptions may require that these modes be explicitly included in V_β, although such an approach is not tested here.

Finally, we consider a simpler model than eq 5 where fluxional modes are treated as uncoupled from one another. To do so we use eqs 5–8 but with eq 5 evaluated for a separable fluxional potential. For $\beta = 3$, for example, such a separable potential is

$$V_3^{\beta\times 1\mathrm{D}}(\varphi_1,\varphi_2,\varphi_3) \equiv V_{1,1}(\varphi_1) + V_{1,2}(\varphi_2) + V_{1,3}(\varphi_3), \tag{10}$$

where the zeroes of energy are defined so that that $V_1(\varphi_i^{\mathrm{eq}}) = 0$, and $V_{1,i}$ is a one-dimensional cut through V_3 along fluxional mode i where all coordinates other than φ_i have been optimized. This is equivalent to describing the set of β fluxional modes via multiple independent 1D corrections, one for each fluxional mode, via β successive one-dimensional applications of eq 6. We label this strategy "β x 1D" to distinguish it from

the coupled βD method, and we note that for a system with one fluxional mode ($\beta = 1$) the two methods are equivalent.

The separable β x 1D model is not always easy to apply. For example, the path obtained via a constrained optimization along a torsional scan may involve an inversion, such that the resulting one-dimensional potentials $V_{1,i}$ computed for the inversion and the torsion are identical. More generally, 1D constrained optimizations can result in identical minima being over or under counted, the results of the scans can depend on starting location and other details of the optimization, and species-specific constraints may need to be implemented. These complications, of course, are a consequence of the nature of fluxional modes and their typically strong coupling to one another, which motivates the βD approach in the first place. It is nonetheless of practical interest to test the β x 1D approach when possible, as this strategy is a common one used in thermochemistry and kinetics. Furthermore, comparing the βx1D and βD results allows us to quantify the physical effect of fluxional mode coupling on anharmonicity.

2.3. Sampling error estimates and high-performance computing scalability

The Monte Carlo sampling procedures used here were described previously.[70,79] Briefly, sampling of the nonfluxional modes was biased toward the bottom of the well, whereas unbiased sampling was used for the fluxional modes in order to fully explore these low-energy motions. In Ref. 79, sample sizes of, typically, $N_{\text{samp}} = 10^6$ to 10^7 were shown to converge Q to better than 1%. Here we consider larger species with up to three fluxional modes and use sample sizes of $N_{\text{samp}} = 10^8$, 10^9, or 10^{10}. We confirmed that Q calculated using N_{samp} differed by less than 3% from Q calculated using $N_{\text{samp}}/10$ for temperatures larger than 500 K for all of the systems studied here. Assuming the usual error scaling with N_{samp}, this suggests errors of less than 1% in the present results.

Due to their more complex structures, some of the systems considered here required large fitting bases such that the resulting analytic potential energy surfaces (PESs) were up to five times more expensive to evaluate than those considered previously.[79] This increase, along with larger values of N_{samp} required here, results in calculations that are up to ~10^3 times more computationally demanding than those from Ref. 79. This challenge was addressed in part using Argonne's petascale computer, Theta,

where a weak scaling parallel efficiency of 82% was achieved on 4,096 nodes (262,144 cores). Typical calculations for this work involved 100–300 nodes and ran for less than two hours.

2.4. Potential energy surfaces

Some of the analytic PESs used here were published previously,[4] with the rest constructed for this work using similar procedures. Briefly, a Metropolis sampling algorithm was employed to generate a set of ab initio energies for each system. These were least-squares-fit using permutationally invariant polynomials[83] constructed as polynomials of Morse variables[84] for all atom–atom distances. Fits of this type are increasingly difficult to accurately parametrize as the size of system increases. The present strategy was found to be suitably efficient for the systems considered here (with as many as 11 atoms) by fully exploiting permutational symmetry. Typically, the CCSD(T)/cc-pVTZ method was used, energies of up to 50 kcal/mol (~17500 cm^{-1}) above the classical minimum were included in the fits, and weights were used to emphasize lower-energy regions.

Fitted critical points reproduced calculated ones to better than a few cm^{-1} for low-lying wells and saddle points. For example, CH_3CHOH has a low-lying secondary local minimum with CCSD(T)/cc-pVTZ and fitted energies of 82.0 and 81.9 cm^{-1}, respectively, relative to the global minimum. Fitting errors were just ~5 cm^{-1} for CH_3CHOH's two inversion saddle points (with CCSD(T)/cc-pVTZ energies of 346.2 and 431.1 cm^{-1}) and just ~3 cm^{-1} for its two lower-energy torsional saddle points (with CCSD(T)/cc-pVTZ energies of 558.0 and 761.8 cm^{-1}). A somewhat larger fitting error (24 cm^{-1}) was found for the higher-energy torsional saddle point at 1493.4 cm^{-1}.

3. Results and Discussion

3.1. Previously computed anharmonicities for systems with zero or one fluxional mode

Rovibrational anharmonicity corrections f for five (0,0) systems, four (0,1) systems, and nine (1,0) systems were calculated in our previous study.[79] These results are re-analyzed here to quantify Γ and Γ' and to test the reduced-dimensional models

described in Sec. 2. Results for these relatively simple systems serve as useful comparisons for the more challenging systems considered in Secs. 3.2 and 3.3.

Nonfluxional species. In Fig. 1, average per-mode anharmonicities Γ are shown for the (0,0) group consisting of H_2O, HO_2, CH_2O, CH_4, and CH_2CH_2, where it can be seen that Γ varies nearly linearly with T and is similar in magnitude for all five species. Using $T' = 1000$ K to define Γ' via eq 4, we find that, averaged over this set of nonfluxional species, $\Gamma'_{(0,0)} = 0.0126 \pm 0.0013$, where 0.0013 is one standard deviation of the five results. Expressed as a percentage, we interpret $\Gamma'_{(0,0)}$ to indicate that, on average, each vibrational mode in a nonfluxional species increases the total rovibrational partition function by 1.26% per 1000 K. The three rotational modes, which carry fractional powers in eqs 3 and 4 and therefore show a more complex temperature dependence, together increase the rovibrational partition function by a factor of $1.90\% = (1.0126^{3/2} - 1) \times 100\%$ at 1000 K.

The narrow distribution of $\Gamma'_{(0,0)}$ for the (0,0) group is perhaps surprising, as $\Gamma'_{(0,0)}$ includes the positive Morse-type anharmonicities typically associated with stretches and often associated with bends as well as anharmonic mode-mode coupling and coupling to overall rotation, which may contribute positively or negatively to the overall anharmonicity. Although the current set of five species is admittedly small, it does feature some variation, including different relative numbers of stretches and bends, atom types, and bond energies. This consistency in Γ' for the (0,0) group allows us to empirically interpret $\Gamma'_{(0,0)} = 1.26 \pm 0.13\%$ as a standard per-mode per-1000 K rovibrational anharmonicity correction for nonfluxional species. This value is summarized in Table 1, where it will be compared with Γ' and $\Gamma'^{\beta D}$ computed for groups of species with fluxional modes, with and without various reduced-dimensional models applied.

We note that the linear dependence shown in Fig. 1 down to low temperatures simplifies our quantification of Γ' and clarifies the present analyses. Despite its usefulness, this behavior is qualitatively incorrect at low temperatures and is in fact an artifact of the present semiclassical approach that effectively allows for fractional (classical) quantum numbers and, in turn, artificial partial excitation of high-frequency

modes at low temperatures. The semiclassical anharmonicity corrections f therefore increase from 1 earlier (i.e., at lower temperatures) than would be observed in more accurate and properly quantized models. Quantitatively, these errors at low temperatures have small absolute magnitudes, which for many applications may be small enough to neglect. At higher temperatures (>1000 K), where the anharmonicity corrections are largest and where the present approaches are most usefully applied, we expect small absolute and small relative errors in f.[55,70,85–87]

Species with one inversion and no torsions. Average per-mode anharmonicities Γ for four (0,1) systems (CH_2, CH_3, NH_3, and CH_2CH) are shown in Fig. 2(a), along with the reference nonfluxional value $\Gamma_{(0,0)}$ quantified above. There is more variation in Γ for the (0,1) group than for the (0,0) group, and CH_3 can be seen as a clear outlier due to the large negative anharmonicity associated with its unhindered umbrella motion. Results for the other three systems are closer in magnitude to the (0,0) reference but show a clear less-than-linear dependence on T. Despite this deviation from linearity, we again quantify these observations using eq 4 and compute $\Gamma'_{(0,1)} = 1.03 \pm 1.50\%$, as summarized in Table 1. The large standard deviation for this group reflects the fact that, as may be expected, the overall anharmonicity correction for a (0,1) species is strongly determined by its fluxional inversion, such that, unlike for the nonfluxional (0,0) group, no useful standard per-mode anharmonicity correction can be derived.

Next, we apply the 1D correction defined by eqs 5 and 6 ($\beta = 1$), and compute the average anharmonicity correction for the remaining nonfluxional modes, Γ^{1D}, using eq 7. The results are shown in Fig. 2(b). With the inversion described by f^{1D}, Γ^{1D} for the remaining modes is found to be in excellent agreement with the nonfluxional reference curve $\Gamma_{(0,0)}$ for three (CH_3, NH_3, and CH_2CH) of the four cases. For these three species, $\Gamma'^{1D}_{(0,1)} = 1.13 \pm 0.20\%$, on average, which is in close agreement with $\Gamma'_{(0,0)} = 1.26 \pm 0.13\%$ quantified for the (0,0) group. If we assume that $\Gamma'_{(0,0)}$ is representative not only of nonfluxional modes in nonfluxional species but also of nonfluxional modes in fluxional species, we can interpret the close agreement of $\Gamma'^{1D}_{(0,1)}$ and $\Gamma'_{(0,0)}$ as indicating that the simple 1D model in eq 5 accurately describes the effect of the inversion on the partition function for three of the four (0,1) systems.

CH_2 is a special case due to the strong coupling of its bending motion with overall rotation. We commented on this in Ref. 78, where we considered the vibrational partition function Q_{vib} along with the rovibrational partition function Q. Typically, the anharmonicity correction factor associated with overall rotational (which can be computed as $Q/Q_{vib}Q_{RR}$) is positive and contributes a factor of $\sim(1 + \Gamma(T))^{3/2}$ to the total rovibrational anharmonicity correction, as built into our definition of Γ in eq 3. For CH_2, however, this factor is less than one, presumably due to strong coupling of the bending mode to overall rotation (e.g., at linear geometries, one of the rotational modes becomes a bending mode). To support this explanation for CH_2, we recomputed Γ'^{1D} using Q_{vib} instead of Q, i.e., with the effect of anharmonic coupling to rotations removed, and again using the 1D model for the CH_2 bend. With this effect removed and as shown in Fig. 2(b), the leftover anharmonicity for the two remaining nonfluxional modes (two C–H stretches) is found to be in quantitative agreement with $\Gamma_{(0,0)}$ and with Γ for the other (0,1) species.

In summary, we interpret these results to indicate that for three of the four species in the (0,1) group, the use of the very simple 1D model for the inversion in eq 5 accurately describes the anharmonicity associated with this fluxional mode. This is demonstrated by the close agreement of Γ^{1D}, the per-mode anharmonicity factor for the remaining nonfluxional modes, with $\Gamma_{(0,0)}$, our reference value for nonfluxional modes. For CH_2, the bend is strongly coupled to overall rotation, and a separable 1D model for the bend is not accurate.

Species with one torsion and no inversions. Six systems with a methyl rotor (CH_3CH, CH_3CO, CH_3OH, CH_3OO, CH_3CHO, and CH_3CH_3) and three other (1,0) systems with a single torsion (H_2O_2, CH_2CHO, and HC(O)OH) were considered in Ref. 79. The rovibrational anharmonicity correction factors f previously computed for these species have been converted to per-mode anharmonicity corrections Γ via eq 3, and these are shown in Fig. 3(a).

There is significant scatter in Γ for the (1,0) systems. Large positive anharmonicities are found for HC(O)OH and CH_2CHOH; these species both feature low-lying secondary minima (higher-energy conformers) that increase their partition functions relative to the single-conformer references used here to define f. In contrast, significant

negative anharmonicities are found for CH_3CO and CH_3CH, both of which feature low torsional barriers and nearly free rotation. The anharmonicity correction factor f is close to zero for the remaining five systems. If, as above, we assume that each nonfluxional mode in these species contributes, on average, $\Gamma'_{(0,0)}$ = 1.26% of positive anharmonicity per 1000 K, values of f near zero at elevated temperatures indicate significant cancellation of the positive anharmonicities associated with *all* of the nonfluxional modes (as many as 20 for C_2H_6) with the negative anharmonicity associated with the *single* torsional mode.

The average per-mode per-1000 K anharmonicity correction for this group, $\Gamma'_{(1,0)}$ = 1.24 ± 2.11%, is close to our nonfluxional reference value $\Gamma'_{(0,0)}$ = 1.26%. The standard deviation of the results, however, is larger than the value itself, again demonstrating the well-known significance of the torsion in determining overall rovibrational properties. Clearly, $\Gamma'_{(1,0)}$ itself is not a useful predictor of anharmonicity for (1,0) species.

The 1D model defined by eq 5 was used to describe the torsion for each species in the (1,0) group, and the resulting per-mode anharmonicity corrections, Γ^{1D}, for the remaining nonfluxional modes are plotted in Fig. 3(b). Despite the significant and varied influence of the torsion apparent in Fig. 3(a), the results in Fig. 3(b) are seen to all increase approximately linearly with temperature and to be clustered around the nonfluxional mode reference curve, $\Gamma_{(0,0)}$. As above when discussing the (0,1) systems, we again interpret the close agreement of Γ^{1D} and $\Gamma_{(0,0)}$ to indicate that the 1D model accurately describes the anharmonicity associated with the torsion.

To quantify this observation, we computed the average and standard deviation of the results in Fig. 3(b), $\Gamma'^{1D}_{(1,0)}$ = 1.08 ± 0.40% (see Table 1), which is in fair agreement with the reference $\Gamma'_{(0,0)}$ = 1.26%. The discrepancy between $\Gamma'^{1D}_{(1,0)}$ and $\Gamma'_{(0,0)}$ may be interpreted as an indicator of the error in the 1D model. We emphasize that this discrepancy is nearly an order of magnitude smaller than $\Gamma'_{(0,0)}$ itself. Using the relationship between f and Γ'^{1D} in eq 8, a difference in of Γ'^{1D} of 1.16 – 1.08 = 0.18 translates into an error estimate for f of just 4% and 10% at 1000 and 2000 K, respectively, for the largest system in the (1,0) group, CH_3CH_3.

Despite the smallness of these errors, we nonetheless consider improvements to

the 1D model in eq 5, and we again quantify the magnitude of each of these improvements via comparisons of the results with the reference value, $\Gamma'_{(0,0)}$. These tests are described next and are intended to provide guidance regarding the optimal balance of computational cost, complexity, and accuracy when implementing reduced-dimensional treatments for systems with complex rovibrational structures at high temperatures.

We first consider the projection correction factor, $\hat{f}$, described by eq 9, designed to approximate the effect of coupling between the fluxional and nonfluxional modes. The $\hat{f}^{1D} = \hat{f} f^{1D}$ model was used to describe the torsion for each of the nine species in (1,0) group, and the resulting per-mode anharmonicities for the remaining nonfluxional modes are shown in Fig. 3(c). The results are again clustered around $\Gamma_{(0,0)}$. In every case, $\hat{f} < 1$, and $\hat{\Gamma}^{1D}$ is therefore increased somewhat relative to Γ^{1D}, with $\hat{\Gamma}'^{1D}_{(1,0)} = 1.18 \pm 0.38\%$ and in better agreement with $\Gamma'_{(0,0)}$ than $\Gamma'^{1D}_{(1,0)}$. The correction factor $\hat{f}$, as defined by eq 9, incorporates some, but not all, of the coupling between the torsion and the remaining nonfluxional modes that is missing in the reduced-dimensional 1D model of eq 5, and it is interesting to note that applying this correction reduces the deviation in the average per-mode anharmonicity for nonfluxional modes from the reference value $\Gamma'_{(0,0)}$ roughly in half. If we again use this deviation and the relationship in eq 8 to estimate the error in f, we can quantify that the use of the projection correction $\hat{f}$ reduces the error in the 1D model by approximately a factor of two, on average.

We emphasize that the magnitude of the $\hat{f}$ correction is small for the species in the (1,0) group, much smaller than the total anharmonicity correction f and the 1D torsional correction f^{1D}. These correction factors are compared in Table 2 at 1000 and 2500 K for the nine (1,0) systems. For just two of the nine cases, $\hat{f}$ has an effect larger than 5% on the total partition function (–16% and –6% for CH_3CO and CH_3CHO), whereas there is much greater variation in f and f^{1D} (–40 to +280% and –56 to +95%, respectively).

The largest deviation of $\hat{f}$ from unity for the species in the (1,0) group is found for CH_3CO ($\hat{f} = 0.84$). This system has the smallest value of $\Gamma'^{1D} = 0.54\%$ and the largest value of $\hat{\Gamma}'^{1D} = 1.92\%$, both of which deviate notably from the reference value $\Gamma'_{(0,0)} = 1.26\%$, suggesting that neither model may be accurate. This system has a low barrier for internal rotation (161 cm^{-1}) and two low normal mode frequencies (99 and 480 cm^{-1})

associated with the torsion and heavy-atom (C–C–O) bend, respectively. The smallness and closeness of these frequencies suggest that they may be coupled and that this system may be more accurately modeled using a two-dimensional reduced-dimensional treatment that included the heavy-atom bend along with the torsion. For comparison, the CH_3CH system has an even lower torsional barrier (115 cm^{-1}), but is better described by the reduced-dimensional 1D models with values of Γ'^{1D} = 0.97% and $\hat{\Gamma}'^{1D}$ = 1.11%, both closer to the reference value $\Gamma'_{(0,0)}$ and showing a clear improvement with the correction factor applied ($\hat{f}$ = 0.98). The better performance of the 1D models for CH_3CH relative to CH_3CO may be attributed to the lighter mass of the terminal atom, which leads to higher and more separated frequencies for the torsion and bend (192 and 776 cm^{-1}, respectively) and presumably smaller coupling between them. These two examples demonstrate the utility of $\hat{f}$ as a diagnostic of the strength of the coupling between the modes included in the reduced-dimensional model and those that are not. When $\hat{f}$ is small it is useful as a quantitative correction factor to f^{1D}, as in the CH_3CH example, while larger values of $\hat{f}$ suggest that additional modes may need to be explicitly coupled to the fluxional ones, as is likely the case for CH_3CO.

Next, we consider improvements to the 1D model via inclusion of geometry-dependent effective moments of inertia (A_i in eq 5) due to internal rotation, as well as the analogous correction to the constants for overall rotation (collectively, B_i). The 1D fluxional model in eqs 5–8 neglects both effects. The correction to A_i in eq 5 appears as $(A/\langle A\rangle)^{1/2}$, where here we have just a single torsion and so we have dropped the subscript i, A is the internal rotational constant evaluated at the equilibrium geometry, and $\langle A\rangle$ is the internal rotational constant properly averaged over the torsional angle. (More precisely, $\langle A\rangle^{-1/2}$ is the Boltzmann-weighted average of $A(\varphi)^{-1/2}$.) This correction factor is shown in Table 2, along with the analogous correction factor to the overall rotational partition function, labeled $(B/\langle B\rangle)^{1/2}$, where B is the product of the three overall rotational constants. For seven of the nine cases, the two correction factors have opposite effects, and they partially cancel each other out. For the five systems considered here with methyl rotors and for H_2O_2, both the individual and total corrections are negligibly small, resulting in less than a 0.5% change to the total partition function at 1000 K. Somewhat larger changes to the overall rotational partition function are found for

HC(O)OH and CH_2CHOH, where including this geometry-dependence decreases the overall rotational partition function by 3 and 10% at 1000 K, respectively. While small, with these corrections applied, $\widehat{\Gamma}'^{1D}_{(1,0)}$ = 1.30 ± 0.32%, in very close agreement with the reference value $\Gamma'_{(0,0)}$, as shown in Table 1. The standard deviation of the results remains somewhat larger for this group than for the (0,0) and (1,0) groups, however.

To summarize the results in Table 2, we emphasize that magnitude of the corrections to the simple 1D model are small, typically much smaller than the 1D correction itself. Together, the corrections affect the total partition function by just 3–4% from 1000 to 2500 K, on average, with just two systems (CH_3CO and CH_2CHOH) having corrections larger than 5%. For CH_3CO, $\hat{f}$ contributes an 18% correction (largely independent of temperature) to the total partition function, which may be interpreted as indicating strong coupling to the low-frequency C–C–O bend, as noted above. For CH_2CHOH, the $(B/\langle B\rangle)^{1/2}$ correction to overall rotational partition function is 11–13% from 1000 to 2500 K. The magnitude of the 1D corrections themselves are much larger, varying from –33 to +95% at 1000 K and from –56% to +75% at 2500 K. Based on the relative magnitudes of the correction factors in Table 2, we can conclude the simplest implementation of the 1D model in eq 5 is may be sufficiently accurate for (1,0) species in many applications.

3.2. Systems with two fluxional modes

Species with one torsion and one inversion. The (1,1) group consists of four species. Two species, CH_2OH and CH_3CH_2, feature CH_2X inversions with low barriers of just 139 and 32 cm^{-1}, respectively. These weakly hindered inversions couple strongly with the torsion; the effect of this coupling on the zero point energy was previously quantified,[4] and its effect on Q was previously discussed qualitatively.[79] We compare results for these species with those for two species featuring NH_2X inversions, which are much more strongly hindered with barriers of 4633 and 2166 cm^{-1} for NH_2OH and CH_3NH_2, respectively. The larger inversion barriers for the N-centered inversions suggest less coupling between the inversion and torsion than for the C-centered inversions, as tested below.

Figure 4(a) shows Γ for the four (1,1) systems. Considerable variation in the

results can be seen, with a per-mode anharmonicity correction as low as –8% at 2500 K for CH_3CH_2 (due to the large negative anharmonicity associated with its nearly free rotor) and as high as +9% at 2500 K for NH_2OH (due to its higher-energy secondary minimum). For CH_2OH and CH_3NH_2, the per mode corrections are closer to zero, and, on average, the anharmonicity corrections for this group are $\Gamma'_{(1,1)}$ = 0.15 ± 4.15%. The dispersion in the results for the (1,1) group is the largest observed so far, again demonstrating that fluxional modes dominate the rovibrational structure. The dispersion in Γ' for the (1,1) group, which features two fluxional modes, is approximately twice as large as was observed for the single-fluxional-mode (0,1) and (1,0) groups.

The torsion and inversion were modeled as coupled to one another and as coupled adiabatically to the remaining modes using the $\hat{f}^{2D}$ model, as defined by eqs 5–9. The anharmonicity corrections associated with the remaining nonfluxional modes, $\hat{\Gamma}^{2D}$, are shown in Fig. 4(b). For all four systems, $\hat{\Gamma}^{2D}$ shows a linear dependence on T with little scatter. On average, $\hat{\Gamma}'^{2D}_{(1,1)}$ = 1.36 ± 0.15% for this group, in close agreement with our nonfluxional reference value $\Gamma'_{(0,0)}$ = 1.26%. The projection correction factor $\hat{f}$ is small for this group and is less than 5% at all temperatures considered for these four systems. Results without $\hat{f}$ applied are not presented in detail; without this correction $\Gamma'^{2D}_{(1,1)}$ = 1.38 ± 0.40%, as shown in Table 1.

The difference between $\hat{\Gamma}'^{2D}_{(1,1)}$ and $\Gamma'_{(0,0)}$ is small, which we interpret to indicate that the projected reduced-dimensional 2D partition function, $\hat{f}^{2D}$, accurately describes the effect of the two coupled fluxional modes on Q. This error is similar in magnitude to (but opposite in sign from) the errors quantified above for the (1,0) and (0,1) groups. Presumably, more sophisticated reduced-dimensional models could further reduce this error, similar to the reductions demonstrated above for the (1,0) group. We do not attempt such tests here. Instead we emphasize that the magnitude of these refinements is likely much smaller than the 2D anharmonicity corrections themselves, while requiring in some cases considerable extra effort. The 2D model, which includes explicit potential coupling between fluxional modes, while neglecting kinetic coupling and treating other potential coupling only approximately, recovers the majority of the anharmonic effects of the fluxional modes despite these simplifications.

It is of interest to test the accuracy of even simpler models in which the two fluxional modes are treated as uncoupled from one another. These models are commonly used, particularly to describe species with multiple torsions, but it is rarely possible to quantify their accuracy, particularly at high temperatures. The present strategy of choosing a model for the fluxional modes and then comparing the "leftover" anharmonicity for the nonfluxional modes with our reference value $\Gamma'_{(0,0)}$ allows for such a test, as detailed next.

The challenge in applying separable 1D corrections for systems with strongly coupled fluxional modes can be seen in Fig. 5, where V_2 for the four (1,1) systems are plotted. For the two CH_2X systems (Figs. 5(a) and 5(b)), the potential energy surfaces show such strong coupling between the torsion and inversion that separate 1D cuts cannot readily be identified. For CH_2OH, one could imagine tracing an optimized torsional path running through all four equivalent minima, but such a path would feature a full inversion cycle along it. Alternatively, one could artificially trace separate torsion and inversion paths that each passed through two of the minima and one saddle point, but these paths would not naturally follow steepest descent or slowest ascent paths without additional constraints. For CH_3CH_2, the coupling is even more pronounced, as the inversion and torsion share a saddle point.

For the two NH_2X systems, in contrast, the potential energy surfaces in Figs. 5(c) and 5(d) show less coupling between the inversion and the torsion, and one can identify clearly separate 1D motions for each of the two modes. These systems illustrate another source of ambiguity when applying separable models for systems with multiple fluxional modes, however. The inversion changes the phase of the torsion, such that, e.g., the minimum torsional angle for NH_2OH is 180° on one side of the inversion and 360° on the other, where, instead, a higher-energy secondary well is found at 180°. One can imagine tracing a torsional path on one side of the inversion that passes through each minimum once and then tracing an inversion path that again passes through each minimum once. Together, these paths would encounter the starting well just once and the secondary well twice, when the true symmetry of the problem has both wells appearing with equal frequency. Furthermore, the results of these paths would depend on which well they were initiated from. This is a common problem that is difficult to address generally,

particularly for systems where the fluxional space cannot be exhaustively explored; this issue may even go unnoticed in some applications, as the energies along the individual paths can appear reasonable.

Here we note that for systems with a single symmetric inversion, we can avoid these ambiguities by restricting the 1D inversion paths to one side of the inversion (e.g., <90°). This is a fair approximation for the NH_2X systems, with their large inversion barriers, but is a poor one for the CH_2X systems, with their strongly coupled motions. This is quantified in Fig. 4(c), where the fluxional modes have been described using the 2x1D model described in Sec. 2, along with the projection correction factor $\hat{f}$, and the per-mode anharmonicity corrections for the remaining nonfluxional modes $\widehat{\Gamma}^{2x1D}$ are plotted. Results for the two NH_2X systems are in close agreement with $\Gamma_{(0,0)}$, indicating that there is no significant error in treating the inversion and torsion as separable motions for these systems. In contrast and as expected from Figs. 5(a) and 5(b), the separable 2x1D description fails qualitatively for the strongly coupled CH_2X systems.

Species with two torsions and no inversions. The (2,0) group consists of seven systems with two torsions, $CH_3CH_2CH_3$, CH_3OCH_3, CH_3CH_2OH, $OC(CH_3)_2$, CH_3OOH, $HOCH_2OH$, and $OC(OH)_2$. As shown in Fig. 6(a), the per-mode anharmonicities, Γ, vary significantly for this group. The two diols both feature low-lying secondary minima and values of $\Gamma > 6\%$ above 1000 K, while $\Gamma < -3\%$ for acetone, which has low torsional barriers. Averaging Γ at 1000 K gives $\Gamma'_{(2,0)} = 2.43 \pm 3.93\%$, where, as observed above for the (1,1) group, the dispersion in the results for this two-fluxional-mode group is approximately twice that for the (0,1) and (1,0) groups.

Next, we test the accuracy of treating the coupled torsions using the projected 2D model. In Fig. 6(b), the per-mode anharmonicities for the remaining nonfluxional modes, $\widehat{\Gamma}^{2D}$, are plotted, and once again they are found to be in good agreement with the nonfluxional mode reference $\Gamma_{(0,0)}$. Averaging the results in Fig. 6(b) at 1000 K gives $\widehat{\Gamma}'^{2D}_{(2,0)} = 1.17 \pm 0.43\%$, again summarized in Table 1, in good agreement with $\Gamma'_{(0,0)} = 1.26\%$ and very close to the result for the single-torsion (1,0) group of species, as shown in Table 1. Presumably, the refinements to the 1D approach tested above for the (1,0) group, such as including geometry dependence in the rotational constants, could further

reduce the discrepancy between $\widehat{\Gamma}'^{2D}_{(2,0)}$ and $\Gamma'_{(0,0)}$, but these refinements are not explored here. The similarity of $\widehat{\Gamma}'^{2D}_{(2,0)}$ and $\widehat{\Gamma}'^{1D}_{(1,0)}$ suggests that the error in the present βD approach scales regularly with the number of modes and that there appears to be no significant additional error for systems with two torsions relative to systems with a single torsion.

The effect of the projection correction factor $\hat{f}$ is larger for this group, on average, than for the groups considered above. These values are summarized in Table 3 along with comparisons of Γ^{2D} and $\widehat{\Gamma}^{2D}$ at 1000 K. For four of the seven systems, $\hat{f}$ represents a correction greater than 10%, and without this correction Γ^{2D} is close to or below zero for these systems, deviating significantly from the reference value, $\Gamma_{(0,0)}$. The most extreme example is acetone, $OC(CH_3)_2$, where $\hat{f}$ = 0.38 and Γ^{2D} = –3.41% before applying the projection correction $\hat{f}$.

When discussing the (1,0) group above, we attributed the large deviation of $\hat{f}$ from unity for CH_3CO to coupling of the torsion to heavy-atom bend. All of the species in the (2,0) group feature such a bend, as one is necessarily formed by the relative motion of the two torsional axes about their shared atom. Just as for the (1,0) group, the presence of such a bend doesn't guarantee a large projection factor correction, however, with $\hat{f}$ deviating from unity by more than 5% for two of four (1,0) species with heavy-atom bends and five of seven (2,0) species.

Table 3 gives the two Cartesian normal mode harmonic frequencies ω most closely associated with the torsions as well as the curvilinear coordinate frequencies $\omega*$ obtained by diagonalizing the Hessian for the reduced-dimensional surface V_2. The ratio of these frequencies is the high-temperature (classical) limit of $\hat{f}$, as indicated by eq 9. Typical differences between ω and $\omega*$ are just a few tens of cm^{-1}. The two systems with one heavy-atom bend and two methyl rotors, $CH_3CH_2CH_3$ and CH_3OCH_3, show the smallest differences between ω and $\omega*$, while the di-ols $HOCH_2OH$ and acetone, $OC(CH_3)_2$ show the largest. The particularly large deviation of $\hat{f}$ from unity for acetone can be attributed to the smallness of its torsional frequencies (ω = 30 and 141 cm^{-1}), such that absolute differences between ω and $\omega*$ of a few tens of cm^{-1} are large relative differences.

The Cartesian normal mode frequencies most closely associated with the heavy-

atom bends, ω_{bend}, are also shown in Table 3. These frequencies are close in magnitude to the torsional frequencies, and in one case, $OC(OH)_2$, are not clearly separated from them. It may be worthwhile to consider improved reduced-dimensional models for fluxional systems where heavy-atom bends are explicitly coupled to the fluxional modes, e.g., by treating them as "fluxional" modes and including them in V_β. Such an approach is not pursued here.

Figure 7 shows V_2 for acetone, where the strong torsional coupling due to very low barriers (242 cm^{-1}) is evident by the rotated axes of the lowest contours. This coupling is also evident by comparing uncoupled and coupled torsional frequencies. Using curvilinear coordinates and treating the two identical torsions as independent, we obtain degenerate torsional frequencies of 125 cm^{-1}. Diagonalizing the 2D projected Hessian splits the degeneracy, giving ω^* = 72 and 161 cm^{-1}. Experimentally, the two lowest frequencies are 77 and 125 cm^{-1},[88] with the coupled 2D treatment clearly improving the description of the lowest-frequency mode. There is a large relative error in the lowest Cartesian normal mode harmonic frequency (ω = 30 cm^{-1}), which can be expected generally for very small frequencies.

Finally, we consider the accuracy of treating the two torsions as separable 1D hindered rotors, which is a widely used approximation for systems with multiple rotors. As indicated by the contour plots in Fig. 8, the four systems with methyl rotors may be expected to show good separability, independent of the identity of the central group (O atom or CH_2) and independent of the identity of the second rotor (CH_3 or OH). Although the contour plots the two di-methyl systems in Figs. 8(a) and (b) look superficially similar to that for $OC(CH_3)_2$ in Fig. 7, the former suggest significantly less torsion–torsion coupling than the latter. This is perhaps most clearly indicated by differences in the first- and second-order saddle points. For the $CH_3CH_2CH_3$ and CH_3OCH_3 systems in Fig. 8, the energies of the second-order saddle points are close to twice that of the first-order ones, as would be expected for uncoupled motions. For acetone, $OC(CH_3)_2$, in contrast, the second-order saddle point energy is more than 3x that of the first-order saddle point. We also note the differences in the 2D curvilinear frequencies for the degenerate torsions. For $CH_3CH_2CH_3$ and CH_3OCH_3, the 2D curvilinear frequencies are split by 30–40 cm^{-1}, whereas this splitting is 90 cm^{-1} for acetone; furthermore, these

splittings represent a change in the frequencies of just 10%–20% for $CH_3CH_2CH_3$ and CH_3OCH_3, relative to the uncoupled 1D frequencies, but 70% for acetone.

Fig. 6(c) shows the result of treating the two torsions using the separable 2x1D approach and including the projection correction $\hat{f}$. As anticipated, results for the 2x1D model are in fair agreement with those for the 2D model in Fig. 6(b) for the species with methyl rotors, aside from acetone, $OC(CH_3)_2$. Table 3 quantifies f^{2D}/f^{2x1D} at two temperatures, where these ratios differ from unity by less than 5% for all but the di-ols and acetone.

Figure 9 shows contour plots for the two di-ols. The contours follow motions that appear rotated by 45°, indicating natural motions where the two OH groups are rotating concertedly either together or in opposite directions. The 360° periodicity for hydroxyl rotors leads to a more complex landscape than species with methyl rotors and their 120° periodicity, with multiple minima and multiple distinct first- and second-order saddle points. Together, these features lead to the observed poorer performance of the 2x1D model for the di-ols than for the species with methyl rotors.

To summarize the results from Sec. 3.2, we note that despite the larger dispersion in Γ for the $\beta = 2$ groups than for the $\beta = 1$ groups, the error in the βD approach remains small for both groups. This is despite the greater likelihood of the fluxional modes coupling strongly to heavy atom bends for $\beta = 2$ than for $\beta = 1$. The separable 2x1D model was shown to perform well for methyl and alkyl rotors and for (1,1) systems with large inversion barriers, but its use resulted in relatively large errors for systems with low-barrier inversions and coupled OH rotors.

3.3. Systems with three fluxional modes

Species with inversions and torsions. One (1,2) system, NH_2NH_2, and three (2,1) systems, CH_3CHCH_3, CH_3CHOH, and HOCHOH, were considered, and their results are analyzed together here. As expected, when no fluxional mode correction is applied, the per-mode anharmonicity corrections vary significantly and feature nonlinear temperature dependence, as shown in Fig. 10(a). The rovibrational anharmonicity corrections for this group vary from strongly negative (–4% per mode) for CH_3CHCH_3, which may be expected to behave similarly to CH_3CH_2, to strongly positive (+10% per mode) for

HOCHOH, which has low-lying secondary minima. On average, $\Gamma'_{(1,2),(2,1)}$= 4.15 ± 4.88%. We note that this value and its standard deviation are larger than those quantified for any of the one- or two-fluxional-mode groups discussed above, as seen in Table 1.

When the $\hat{f}^{3D}$ model is used to describe the three fluxional modes, the resulting per-mode anharmonicities for the remaining nonfluxional modes, $\widehat{\Gamma}^{3D}$, are once again found to be in good agreement with the $\Gamma_{(0,0)}$ reference, as shown in Fig. 10(b). The curves vary nearly linearly with temperature, and $\widehat{\Gamma}'^{3D}_{(2,1),(1,2)}$ = 1.14 ± 0.23. Despite the good agreement of this value with $\Gamma'_{(0,0)}$ and the small dispersion in the results, we note that for all four systems, the Cartesian normal mode frequencies associated most closely with the fluxional modes are not clearly separated from the nonfluxional ones. This leads to some ambiguity in the application of the $\hat{f}$ correction in the $\hat{f}^{3D}$ model, as discussed next.

For NH_2NH_2, the four lowest Cartesian normal mode frequencies computed using our fitted PES are ω = 401, 864, 1046, and 1128 cm^{-1}. The lowest-energy mode is clearly associated with the torsion, and the 3rd frequency, when visualized, may be unambiguously assigned as an antisymmetric linear combination of the two –NH_2 inversions. The motions associated with the 2nd and 4th frequencies are similar, however, with both showing some character of the symmetric combination of the inversions as well as some character of the N–N stretch. Note that the average of the 2nd and 4th frequencies is close to the 3rd, further suggesting that coupling to the N–N stretch has split the frequency associated with the symmetric combination of inversions away from a value more similar to that of the antisymmetric combination.

The N–N stretch was not included in our reduced-dimensional 3D fluxional model, and the three frequencies calculated using V_3 therefore do not include the splitting arising from coupling to the N–N mode. Instead, ω^* = 404, 1006, and 1012 cm^{-1}. The computation of our projection correction $\hat{f}$ is therefore ambiguous, as it is unclear which Cartesian normal mode frequency to assign as the 2nd inversion. We chose to set this frequency to the average of the 2nd and 4th frequencies, which resulted in a value of $\widehat{\Gamma}^{3D}$ for NH_2NH_2 that is in good agreement with $\Gamma'_{(0,0)}$; it is not clear that such an approach can be relied upon generally. A more rigorous approach may require expanding the

number of modes included in V_β to include the N–N stretch.

For the three (2,1) systems, all of which feature an X–CH–Y inversion, the Cartesian normal mode frequency associated the heavy-atom bend is intermediate of the three fluxional frequencies. Coupling of the bend to the inversion is strongest for CH_3CHCH_3, where the four lowest frequencies are ω = 113, 140, 345, and 403 cm^{-1}, with motions associated with the 3rd and 4th frequencies both including significant bending character. Coupling is weakest for HOCHOH, where ω = 277, 361, 540, and 958 cm^{-1}, with the bend at 540 cm^{-1} separated from the inversion at 958 cm^{-1} and the torsions at 361 cm^{-1} and below. CH_3CHOH is an intermediate case, with ω = 186, 366, 407, and 611 cm^{-1}. For all three species, we chose to use the 1st, 2nd, and 4th Cartesian normal mode frequencies in our application of $\hat{f}$. With this choice, $\hat{f}$ = 0.85 for CH_3CHCH_3 (T > 500 K) indicating that a more rigorous approach may require expanding the number of modes included in V_β to include the C–C–C bend. For CH_3CHOH and HOCHOH, $\hat{f}$ = 0.97 (T > 500 K), but the ambiguity in the assignment of Cartesian frequencies as fluxional modes again suggests strong coupling to the heavy atom bend.

The (2,1) systems share features with both the (1,1) and (2,0) groups, as evident in the contour plots shown in Figs. 11 and 12. There considerable complexity in the 3D space of fluxional modes, including multiple low-energy minima and first- and second-order saddle points. For CH_3CHCH_3, the inversion and torsion are strongly coupled (cf. Fig. 11(a)), as was the case for CH_3CH_2. HOCHOH, in contrast, has a fairly large barrier to inversion, but its two OH rotors are strongly coupled (cf. Fig. 11(d)), as was the case for the di-ols in the (2,0) group. CH_3CHOH is an intermediate case, and one can identify strong coupling between the inversion and OH torsion, as noted above for CH_2OH in Fig. 12(b).

We tested the use of the fully separable 3x1D model for the (1,2) and (2,1) species, and the resulting values of $\hat{\Gamma}^{3\times1D}$ are shown in Fig. 10(c) and given in Table 1. These calculations considered just half of each inversion when computing its 1D correction, as motivated above when discussing the (1,1) group. As expected from Figs. 11 and 12, the fully separable 3x1D model performs poorly for these systems.

Species with three torsions. Three (3,0) systems were studied: $HOCH_2CH_2OH$, CH_3OOCH_3, and $HC(OH)_3$. Figure 13(a) shows Γ for this group, which includes both

large positive and negative anharmonicity corrections, and $\Gamma'_{(3,0)}$ = 4.09 ± 4.57%, on average. Notably, the average and dispersion in $\Gamma_{(3,0)}$ is similar to those quantified for the (1,2) and (2,1) species. As seen in Table 1, increasing the number of fluxional modes generally leads to larger anharmonicity corrections, on average, but, even more importantly, these corrections become more and more difficult to anticipate as indicated by the increasing dispersion in Γ with β.

In Fig. 13(b), the $\hat{f}^{3D}$ model has been used to describe the three torsions, and the leftover per-mode anharmonicities for the remaining nonfluxional modes $\widehat{\Gamma}^{3D}$ are shown. This correction results in curves that show a fairly linear temperature dependence and that are close to but somewhat larger than the $\Gamma_{(0,0)}$ reference curve, with $\widehat{\Gamma}^{3D}_{(3,0)}$ = 1.40 ± 0.20%. We again note some ambiguity when applying the $\hat{f}$ model, as the torsional frequencies for these three systems are not well separated from the frequencies for the heavy-atom bends. This is likely a general result, with the $\hat{f}$ model increasingly difficult to apply for large system where fluxional modes are less and less likely to be well separated from nonfluxional ones. When the projection correction is not applied, the results are found to be in closer agreement with $\Gamma_{(0,0)}$ for this group, with $\Gamma^{3D}_{(3,0)}$ = 1.25 ± 0.09%.

Figure 13(c) shows the result of treating the three torsions using the projected 3x1D model, i.e., as independent 1D rotors and applying the $\hat{f}$ correction. The independent rotor approximation introduces very little error for CH_3OOCH_3, which is readily rationalized by the separable torsional paths evident in the contour plots in Fig. 14.

Multiple OH rotors lead to stronger coupling and more complex potential energy surfaces, as was observed above for the di-ols in the (2,0) and (2,1) groups. For the tri-ol $CH(OH)_3$, strong coupling of the OH rotors is evident in Fig. 15. $HOCH_2CH_2OH$ is a more interesting case, where the OH rotors are clearly strongly coupled to one another when in its "gauche" configuration (Fig. 16(a)) but much less coupled when in the "anti" configuration (Fig. 16(b)), i.e., the strength of the OH coupling itself is coupled to the internal alkyl rotor. Neither multi-ol system is well represented by the 3x1D model.

3.4. Summary of errors in Q

Throughout Secs. 3.1–3.3, per-mode anharmonicities were used to quantify the impact of different types of fluxional modes as well as to judge the performance several reduced-dimensional models. Here we convert this information from per-mode errors to errors in the total rovibrational partition function. This analysis is intended to give a more intuitive feeling for the errors identified throughout this work.

We use the full-dimensional, fully coupled MCPSI values of f as benchmarks, and we test the performance of several different combinations of models for the fluxional modes, f_F, and for the nonfluxional modes, f_{NF}. In our first set of tests, we consider $f_F = \hat{f}^{\beta D}$, $f^{\beta D}$, or $\hat{f}^{\beta \times 1D}$, and we assume that nonfluxional modes are well described, on average, by the standard value $\Gamma_{(0,0)}$, i.e.,

$$f_{NF} = f_{(0,0)} = [1 + \Gamma_{(0,0)}(T)]^{\alpha-\beta-3/2}, \tag{11}$$

where α and β are the numbers of total rovibrational modes and fluxional modes, respectively. For each of the thirty-six systems, we computed the error $f_F f_{NF} - f$, which is the relative error (reported as a percentage error) in the predicted rovibrational anharmonic partition function. These errors were averaged for several different groups of species, and their mean and one-sigma standard deviation are reported in Table 4 at 1000 and 2500 K. We emphasize that this analysis relies on two assumptions: (1) that nonfluxional modes behave uniformly, on average, according to eq 11, and (2) that any deviation of $f_F f_{NF}$ from f may be attributed as an error in the model for f_F.

As discussed throughout Sec. 3 and as shown in Table 4, the error in the $\hat{f}^{\beta D}$ method performs well for all of the groups considered here, although we note approximately twice as much error for $\beta = 2$ and 3 groups than for $\beta = 1$ groups, on average. The error in the $\hat{f}^{\beta D}$ approach is small when averaged over all thirty-six systems and is just 0 ± 10% and –3 ± 15% at 1000 and 2500 K, respectively. We may further condense this information into a single error estimate (labeled ~2σ in Table 4) by adding the absolute value of the mean error to twice the standard deviation and then averaging over the two temperatures. Doing so for the $\hat{f}^{\beta D}$ method gives a ~2σ error estimate of just 27%, as shown in Table 4.

The small magnitude of this error is notable, as in many kinetics applications

errors of this size will typically be smaller than or similar to other sources of error,[89–91] such as those associated with practical treatments for computing tunneling,[92] collisional energy transfer,[93] and/or threshold energies.[94] Furthermore, the magnitude of this error is competitive with experimental error bars assigned in many kinetics studies, thus further validating a priori theory, alongside experiment, as an independent source of kinetic and thermochemical information.

The smallness of the error in the $\hat{f}^{\beta D}$ method is also notable in that the βD model used here is fairly simple in its implementation. By sampling the fluxional coordinates and Boltzmann-averaging the resulting partially-optimized potential energies, and avoiding any sophisticated treatments of kinetic couplings, the fluxional modes are already shown to be very accurately described. While more complicated implementations can further reduce the error, as demonstrated above for a few such implementations, the magnitude of the reductions may be expected generally to be quite small; the simplest approaches may be sufficiently accurate for many applications.

The neglect of coupling *between* fluxional modes, as in the $\hat{f}^{\beta\times 1D}$ model and as is commonly employed, is a severe approximation, with errors, on average, as large as 17 ± 148% at 2500 K (~2σ = 249%), as shown in Table 4. For the systems considered here different fluxional motions in a given species typically involve the same atoms, and so the strong coupling among these fluxional modes is not surprising. It is interesting to note that the separable βx1D approach performs notably better at 1000 K than at 2500 K and performs fairly well for $\beta = 2$. These results may explain, in part, the perceived success of this widely used approach, which is most likely to be tested at lower temperatures and for smaller systems.

The errors in the $\hat{f}^{\beta D}$, $f^{\beta D}$, and $\hat{f}^{\beta\times 1D}$ methods may be compared with the error in the simple single-well RRHO approximation used here as our reference for f; this approach is labeled f_{RRHO} in Table 4. A more complete RRHO approximation might include sums of RRHO partition function for every well in the system, but such an approach is not tested here. In the context of the present error analysis, the single-well RRHO approximation is equivalent to setting $f_F = 1$ and $f_{NF} = 1$. As expected, this approximation systematically underestimates rovibrational anharmonicity and the magnitude of the error increases with temperature. When averaged over all thirty-six systems, ~2σ = 355% for this RRHO

method, which is notably not too dissimilar from the error assigned to the separable βx1D approach. These values of ~2σ suggest that there may be only marginal gain in applying the much more complicated and computationally demanding βx1D approach than simply using the RRHO approach. Of course, this result is system-dependent, but we note it to emphasize the straightforward point that more complicated calculations are not necessarily worth the effort. Realistic error estimates, such as the values of ~2σ in Table 4, are required to usefully make judgements about the optimal compromise of computational cost and accuracy.

Finally, we compare results for two approaches where the anharmonicity associated with the nonfluxional modes is neglected entirely, i.e., where we have set f_{NF} = 1. We label these methods $\hat{f}^{\beta\mathrm{D}}f_{\mathrm{RRHO}}$ and $\hat{f}^{\beta\mathrm{x1D}}f_{\mathrm{RRHO}}$ in Table 4. Comparing the $\hat{f}^{\beta\mathrm{D}}f_{(0,0)}$ and $\hat{f}^{\beta\mathrm{D}}f_{\mathrm{RRHO}}$ results allows us to comment on the importance of the nonfluxional modes in determining the overall anharmonicity. The $\hat{f}^{\beta\mathrm{D}}f_{\mathrm{RRHO}}$ method performs very poorly, with ~2σ = 164%, demonstrating that, again averaged over all the systems considered here, the cumulative anharmonicity associated with the nonfluxional modes is a significant component of the overall anharmonicity and cannot be quantitatively neglected at elevated temperatures. Unlike the anharmonicity in the fluxional modes, the anharmonicity associated with the nonfluxional modes has a consistent (positive) sign, and so approximate approaches can benefit from a cancelation of errors. This is perhaps seen in the results for the $\hat{f}^{\beta\mathrm{x1D}}f_{\mathrm{RRHO}}$ method, where the positive systematic errors for the $\hat{f}^{\beta\mathrm{x1D}}f_{(0,0)}$ method for some groups are lowered when using the $\hat{f}^{\beta\mathrm{x1D}}f_{\mathrm{RRHO}}$ method. The $\hat{f}^{\beta\mathrm{x1D}}f_{\mathrm{RRHO}}$ method has been widely applied in gas phase kinetics, and this cancellation, along with the method's fair accuracy at lower temperatures and for β = 2, likely explains, in part, its relative success. The present comparisons suggest that this cancellation of errors may not be reliable for larger systems.

4. Conclusions

Full-dimensional fully-coupled semiclassical rovibrational anharmonicity corrections f were computed and analyzed for several species with up to three fluxional modes. This set of results was used to quantify the importance of fluxional modes in

determining rovibrational properties at high temperatures as well as to test the accuracy of reduced-dimensional approaches. We showed that as the number of fluxional modes increases, the magnitude of their impact increases and, more importantly, these effects become more and more difficult to anticipate.

We showed that a fairly simple βD reduced-dimensional approach where all β of the fluxional modes are coupled to one another but as uncoupled from the nonfluxional modes generally performs well, with a derived two-sigma error estimate at high temperatures (>1000 K) of just ~2σ = 27%. More detailed implementations of the βD approach were tested, and, although these studies generally led to improved results, the already small errors for the simplest βD approach suggests that more complicated implementations may not be worth the extra computational cost and complexity.

Although we have emphasized the testing of reduced-dimensional models throughout this work, we note that one could instead simply compute f in its full-dimensionality without approximation. The present work demonstrates that such applications are possible for fairly complex systems with up to eleven atoms and three fluxional modes. The present calculations benefitted from access to high performance computing resources and employed fitted potential energy surfaces to converge f to ~1%. In more practical applications, where such small statistical uncertainties are not needed, MCPSI calculations may be possible using direct (on-the-fly) implementations.

We note also the approach described by us in Ref. 71 where the full-dimensional MCPSI integral for Q is replaced by convolutions of many lower-dimensional ones. This approach is expected to scale favorably with system size, and this approach is currently being explored as means of avoiding the need for reduced dimensional strategies.

Although the βD method performs well, several ambiguities in its implementation were pointed out, and one expects these ambiguities to become more and more prevalent for larger systems. We noted the increasing difficulty in separating the fluxional modes from the nonfluxional ones, and we specifically highlighted the prevalence of low-frequency bends that appeared to be coupled strongly to inversions and torsions. By comparing Cartesian normal mode frequencies with reduced-dimensional (i.e., projected) curvilinear ones, we showed that $\hat{f}$ was sometimes diagnostic of this coupling.

Central to our analysis was the identification of a standard per-mode

anharmonicity parameter $\Gamma_{(0,0)}$ for nonfluxional modes. This value was quantified to be 1.26% per vibrational mode per 1000 K. While this anharmonicity is much more reliably estimated than the anharmonicity associated with the nonfluxional modes, we note that it is often neglected entirely in practical applications as it has fairly small per-mode contribution relative to fluxional modes. Because of the relatively larger number of nonfluxional modes, however, they can comprise a significant fraction of the overall anharmonicity, particularly at high temperatures.

Acknowledgments

This work was supported by the U. S. Department of Energy, Office of Basic Energy Sciences, Division of Chemical Sciences, Geosciences, and Biosciences and used resources of the Argonne Leadership Computing Facility, which is a DOE Office of Science User Facility, operating under Contract Number DE-AC02-06CH11357. This research was supported in part by the Exascale Computing Project (ECP), Project Number: 17-SC-20-SC, a collaborative effort of two DOE organizations, the Office of Science and the National Nuclear Security Administration, responsible for the planning and preparation of a capable exascale ecosystem including software, applications, hardware, advanced system engineering, and early test bed platforms to support the nation's exascale computing imperative.

Table 1. Rovibrational anharmonicity corrections per mode and per 1000 K

(N_t,N_i)	Systems[a]	Γ', %	$\widehat{\Gamma}'^{\beta D}$, %	$\Gamma'^{\beta D}$, %	$\widehat{\Gamma}'^{\beta \times 1D}$, %
(0,0)	*H_2O, HO_2, CH_2O, CH_4, CH_2CH_2*	1.26 ± 0.13			
(0,1)	*CH_2, CH_3, NH_3, CH_2CH*	1.03 ± 1.50	1.04 ± 0.12[b]	1.13 ± 0.20[b]	c
(1,0)	*H_2O_2, CH_3OH, CH_3CH, CH_3CO, CH_3OO, CH_3CHO, CH_3CH_3, $HC(O)OH$, CH_2CHOH*	1.24 ± 2.11	1.18 ± 0.38	1.08 ± 0.40	c
(1,1)	*CH_2OH, CH_3CH_2, NH_2OH,* CH_3NH_2	0.15 ± 4.15	1.36 ± 0.15	1.38 ± 0.40	–2.29 ± 2.55
(2,0)	$CH_3CH_2CH_3$, $OC(OH)_2$, CH_3CH_2OH, CH_3OOH, $HOCH_2OH$, CH_3OCH_3, $OC(CH_3)_2$	2.43 ± 3.93	1.17 ± 0.43 [1.26 ± 0.39][d]	0.03 ± 1.58 [0.61 ± 0.47][d]	1.13 ± 0.38 [1.00 ± 0.18][d]
(1,2), (2,1)[e]	*NH_2NH_2,* CH_3CHCH_3, HOCHOH, CH_3CHOH	4.15 ± 4.88	1.13 ± 0.23	0.82 ± 0.52	–1.61 ± 2.47
(3,0)	CH_3OOCH_3, $HC(OH)_3$, $HOCH_2CH_2OH$	4.09 ± 4.57	1.40 ± 0.20	1.25 ± 0.09	–1.22 ± 2.93

[a]Italics indicate anharmonicity corrections taken from Ref. 79.

[b]CH_2 is atypical and was excluded from these results. See text for details.

[c]The 1D and βD models are equivalent for these groups.

[d]$OC(CH_3)_2$ is atypical and was excluded from the results in brackets. See text for details.

[e]These results include both the (1,2) and (2,1) groups.

Table 2. Correction factors to the total partition function at two temperatures for nine (1,0) systems[a]

System	T, K	f	f^{1D}	$\hat{f}$	$(A/\langle A\rangle)^{1/2}$	$(B/\langle B\rangle)^{1/2}$
CH_3OH	1000	**1.183**	1.019	1.000	0.999	1.001
	2500	**1.117**	**0.748**	1.000	0.998	1.001
CH_3CH	1000	**0.751**	**0.665**	0.982	0.996	1.003
	2500	**0.605**	**0.442**	0.981	0.996	1.003
CH_3CO	1000	**0.815**	**0.762**	**0.844**	1.004	0.997
	2500	**0.744**	**0.515**	**0.837**	1.004	0.997
CH_3OO	1000	**1.177**	0.982	1.037	0.999	0.995
	2500	**1.141**	**0.709**	1.039	0.999	0.994
CH_3CHO	1000	**1.156**	1.031	**0.941**	1.001	1.004
	2500	**1.139**	**0.763**	**0.937**	1.001	1.005
CH_3CH_3	1000	**1.399**	**1.173**	1.005	0.999	1.000
	2500	**1.673**	1.024	1.006	0.999	1.000
H_2O_2	1000	**1.159**	1.027	1.017	1.002	0.996
	2500	**1.115**	**1.750**	1.020	1.002	0.996
HC(O)OH	1000	**1.329**	**1.196**	1.035	1.000	0.970
	2500	**2.278**	**0.849**	1.048	1.002	**0.904**
CH_2CHOH	1000	**2.223**	**1.952**	1.006	1.004	**0.895**
	2500	**3.799**	**1.132**	1.007	1.013	**0.869**
average	1000	1.24 ± 0.42	1.09 ± 0.37	0.99 ± 0.06	1.00 ± 0.00	0.98 ± 0.04
	2500	1.51 ± 0.99	0.88 ± 0.39	0.99 ± 0.06	1.00 ± 0.00	0.97 ± 0.05

[a]Corrections larger than 5% are shown in bold.

Table 3. Projection and anharmonicity corrections at 1000 K, fluxional frequencies (cm^{-1}), and ratios of the 2D and 2x1D corrections at two temperatures for the (2,0) group

System	$\hat{f}$	Γ^{2D}	$\hat{\Gamma}^{2D}$	ω^*	ω	ω_{bend}	$f^{2D}/f^{2\times1D}$ 1000 K	2000 K
CH_3OCH_3	0.98	1.13%	1.24%	213, 254	203, 260	420	0.992	0.995
$CH_3CH_2CH_3$	0.96	0.73	0.88	234, 264	216, 274	362	0.963	0.970
$OC(OH)_2$	0.94	1.15	1.73	543, 650	529, 600	546,602	0.902	0.864
CH_3OOH	0.87	0.08	1.03	193, 308	195, 258	449	1.012	0.997
CH_3CH_2OH	0.86	0.18	0.92	271, 294	236, 281	412	1.031	1.015
$HOCH_2OH$	0.82	0.36	1.75	398, 472	377, 379	586	0.904	0.712
$OC(CH_3)_2$	0.38	–3.41	0.62	72, 161	30, 141	372,479	1.346	1.404

Table 4. Errors (%) in the rovibrational partition function Q at two temperatures[a]

Group	$\hat{f}^{\beta D} f_{(0,0)}$	$f^{\beta D} f_{(0,0)}$	$\hat{f}^{\beta \times 1D} f_{(0,0)}$	f_{RRHO}	$\hat{f}^{\beta D} f_{RRHO}$	$\hat{f}^{\beta \times 1D} f_{RRHO}$
all	0 ± 10	8 ± 15	2 ± 92	–56 ± 113	–25 ± 33	–23 ± 93
	–3 ± 15	7 ± 20	17 ± 148	–90 ± 169	–69 ± 84	–53 ± 143
~2σ[b]	27	42	249	355	164	275
$\beta = 1$	3 ± 6	4 ± 5	3 ± 6	–20 ± 36	–14 ± 6	–14 ± 6
	0 ± 8	1 ± 8	0 ± 8	–42 ± 83	–42 ± 36	–42 ± 36
2	1 ± 10	18 ± 22	13 ± 18	–49 ± 78	–26 ± 18	–16 ± 25
	–6 ± 24	18 ± 30	27 ± 52	–103 ± 162	–79 ± 64	–57 ± 53
3	–4 ± 18	6 ± 10	–16 ± 219	–169 ± 206	–55 ± 64	–62 ± 218
	–5 ± 13	7 ± 18	45 ± 347	–203 ± 293	–130 ± 157	–87 ± 332
(0,0)	0 ± 1	0 ± 1	0 ± 1	–11 ± 5	–11 ± 5	–11 ± 5
	0 ± 3	0 ± 3	0 ± 3	–29 ± 17	–29 ± 17	–29 ± 17
(0,1)	1 ± 1	2 ± 3	1 ± 1	–9 ± 13	–8 ± 3	–8 ± 3
	0 ± 5	3 ± 4	0 ± 5	–22 ± 23	–23 ± 11	–23 ± 11
(1,0)	3 ± 7	4 ± 6	3 ± 7	–24 ± 42	–16 ± 6	–16 ± 6
	0 ± 9	0 ± 9	0 ± 9	–51 ± 99	–51 ± 40	–51 ± 40
(1,1)	0 ± 1	0 ± 6	21 ± 29	–8 ± 51	–14 ± 6	5 ± 30
	–4 ± 7	–5 ± 17	22 ± 38	–30 ± 91	–39 ± 26	–21 ± 48
(2,0)	1 ± 13	29 ± 21	8 ± 9	–73 ± 85	–33 ± 19	–28 ± 11
	–8 ± 30	31 ± 29	30 ± 61	–144 ± 184	–102 ± 70	–77 ± 47
(1,2),	3 ± 6	11 ± 10	87 ± 62	–112 ± 125	–30 ± 17	39 ± 59
(2,1)	–2 ± 10	4 ± 13	184 ± 228	–114 ± 128	–71 ± 41	54 ± 163
(3,0)	–14 ± 25	0 ± 3	–153 ± 298	–244 ± 298	–90 ± 94	–196 ± 299
	–10 ± 19	11 ± 25	–142 ± 439	–322 ± 442	–208 ± 235	–274 ± 445

[a]Each entry shows the average and one standard deviation for the group. Results at 1000 K are shown above results at 2500 K.

[b]A two-sigma error (%) was estimated as the absolute value of the mean error plus twice the standard deviation, averaged over the two temperatures.

References

[1] Pilling, M. J. Reactions of Hydrocarbon Radicals and Biradicals. *J. Phys. Chem. A* **2013**, *117*, 3697–3717.

[2] Klippenstein, S. J. From Theoretical Reaction Dynamics to Chemical Modeling of Combustion. *Proc. Comb. Inst*. **2017**, *36*, 77–111.

[3] McCoy, A. B. Diffusion Monte Carlo Approaches to Investigating the Structure and Vibrational Spectra of Fluxional Systems. *Int. Rev. Phys. Chem.* **2006**, *25*, 77–107.

[4] Harding, L. B.; Georgievski, Y.; Klippenstein, S. J. Accurate Anharmonic Zero Point Energies for some Combustion Related Species from Diffusion Monte Carlo, *J. Phys. Chem. A*, **2017**, *121*, 4334–4340.

[5] Carney, G. D.; Sprandel, L. I.; Kern, C. W. Variational Approaches to the Vibration-Rotation Spectroscopy for Polyatomic Molecules. *Adv. Chem. Phys.* **1978**, 37, 305–380.

[6] Bowman, J. M. Self-Consistent Field Energies and Wavefunctions for Coupled Oscillators. *J. Chem. Phys.* **1978**, *68*, 608−610.

[7] Bowman, J. M.; Christoffel, K.; Tobin, F. Application of SCF-SI Theory to Vibrational Motion in Polyatomic Molecules. *J. Phys. Chem.* **1979**, *83*, 905−912.

[8] Carter, S.; Bowman, J. M.; Handy, N. C. Extensions and Tests of "Multimode": A Code to Obtain Accurate Vibration/Rotation Energies of Many-Mode Molecules. *Theor. Chem. Acc.* **1998**, *100*, 191–198.

[9] Tew, D. P.; Handy, N. C.; Carter, S. A Reaction Surface Hamiltonian Study of Malonaldehyde. *J. Chem. Phys.* **2006**, *125*, 084313.

[10] Chakraborty, A.; Truhlar, D. G. Converged Vibrational Energy Levels and Quantum Mechanical Vibrational Partition Function of Ethane, *J. Chem. Phys.* **2006**, *124*, 184310.

[11] Njegic, B.; Gordon, M. S. Exploring the Effect of Anharmonicity of Molecular Vibrations on Thermodynamic Properties. *J. Chem. Phys.* **2006**, *125*, 224102.

[12] Begue, D.; Gohaud, N.; Pouchan, C. A Comparison of Two Methods for Selecting Vibrational Configuration Interaction Spaces on a Heptatomic System: Ethylene oxide. *J. Chem. Phys.* **2007**, *127*, 164115.

[13] Keçeli, M.; Shiozaki, T.; Yagi, K.; Hirata, S. Anharmonic Vibrational Frequencies and Vibrationally Averaged Structures of Key Species in Hydrocarbon Combustion: HCO^+, HCO, HNO, HOO, HOO^-, CH_3^+, and CH_3. *Mol. Phys.* **2009**, *107*, 1283–1301.

[14] Keçeli, M.; Hirata, S. Size-Extensive Vibrational Self-Consistent Field Method. *J. Chem. Phys.* **2011**, *135*, 134108.

[15] Yagi, K.; Keçeli, M.; Hirata, S. Optimized Coordinates for Anharmonic Vibrational Structure Theories. *J. Chem. Phys.* **2012**, *137*, 204118.

[16] Faucheaux, J. A.; Hirata, S. Higher-Order Diagrammatic Vibrational Coupled-Cluster Theory. *J. Chem. Phys.* **2015**, *143*, 134105.

[17] Ceperley, D. Path Integrals in the Theory of Condensed Helium. *Rev. Mod. Phys.* **1995**, *67*, 279–355.

[18] Berne, B. J.; Thirumalai, D. On the Simulation of Quantum Systems: Path Integral Methods. *Annu. Rev. Phys. Chem.* **1986**, *37*, 401–424.

[19] Mielke, S. L.; Srinivasan, J.; Truhlar, D. G. Extrapolation and perturbation schemes for accelerating the convergence of quantum mechanical free energy calculations via the Fourier path-integral Monte Carlo method. *J. Chem. Phys.* **2000**, *112*, 8758–8764.

[20] Mielke, S. L.; Truhlar, D. G. Displaced-Points Path Integral Method for Including Quantum Effects in the Monte Carlo Evaluation of Free Energies. *J. Chem. Phys*. **2001**, *115*, 652–662.

[21] Miller, T. F. III; Clary, D. C. Torsional Path Integral Monte Carlo method for calculating the absolute quantum free energy of large molecules, *J. Chem. Phys.* **2003**, *119*, 68–76.

[22] Sturdy, Y. K.; Clary, D. C. Torsional Anharmonicity in Transition State Theory Calculations. *Phys. Chem. Chem. Phys.* **2007**, 2397–2405.

[23] Mielke, S. L.; Truhlar, D. G. Improved Methods for Feynman Path Integral Calculations of Vibrational–Rotational Free Energies and Application to Isotopic Fractionation of Hydrated Chloride Ions. *J. Phys. Chem. A* **2009**, *113*, 4817–4827.

[24] Mielke, S. L.; Truhlar, D. G. Improved Methods for Feynman Path Integral Calculations and their Application to Calculate Converged Vibrational–Rotational

Partition Functions, Free Energies, Enthalpies, Entropies, and Heat Capacities for Methane. *J. Chem. Phys.* **2015**, *142*, 044105.

[25] Light, J. C.; Hamilton, I. P.; Lill, J. V. Generalized Discrete Variable Approximation in Quantum Mechanics. *J. Chem. Phys.* **1985**, *82*, 1400–1409.

[26] Tennyson, J. The Calculation of the Vibration-Rotation Energies of Triatomic Molecules Using Scattering Coordinates, *Comput. Phys. Rep.* **1986**, *4*, 1–36.

[27] Carter, S.; Handy, N. C. A Variational Method for the Determination of the Vibrational (J = 0) Energy Levels of Acetylene, using a Hamiltonian in Internal Coordinates. *Comput. Phys. Commun.* **1988**, *51*, 49–58.

[28] Chen, R.; Ma, G.; Guo, H. Six-Dimensional Quantum Calculations of Highly Excited Vibrational Energy Levels of Hydrogen Peroxide and its Deuterated Isotopomers. *J. Chem. Phys.* **2001**, *114*, 4763–4774.

[29] Fabri, C.; Matyus, E.; Furtenbacher, T.; Nemes, L.; Mihaly, B.; Zoltani, T.; Csaszar, A. Variational Quantum Mechanical and Active Database Approaches to the Rotational-Vibrational Spectroscopy of Ketene, H_2CCO. *J. Chem. Phys.* **2011**, 135, 094307.

[30] Christiansen, O. Selected New Developments in Vibrational Structure Theory: Potential Construction and Vibrational Wave Function Calculations. *Phys. Chem. Chem. Phys.* **2012**, *14*, 6672−6687.

[31] Wodraszka, R.; Manthe, U. Iterative Diagonalization in the Multiconfigurational Time-Dependent Hartree Approach: Ro-vibrational Eigenstates. *J. Phys. Chem. A* **2013**, *117*, 7246–7255.

[32] Halverson, T.; Poirier, B. Large Scale Exact Quantum Dynamics: Ten Thousand Quantum States of Acetonitrile. *Chem. Phys. Lett.* **2015**, *624*, 37–42.

[33] Yu, H.-G. An Exact Variational Method to Calculate Rovibrational Spectra of Polyatomic Molecules with Large Amplitude Motion. *J. Chem. Phys.* **2016**, *145*, 084109.

[34] Carrington, T. Perspective: Computing (Ro-)Vibrational Spectra of Molecules with More than Four Atoms. *J. Chem. Phys.* **2017**, *146*, 120902.

[35] Avila, G.; Carrington, T. Computing Vibrational Energy Levels of CH_4 with a Smolyak Collocation Method. *J. Chem. Phys.* **2017**, *147*, 144102.

[36] Troe, J. Simplified Models for Anharmonic Numbers and Densities of Vibrational States. I. Application to NO_2 and H_3^+. *Chem. Phys.* **1995**, *190,* 381–392.

[37] Schmatz, S. Approximate Calculation of Anharmonic Densities of Vibrational States for Very Large Molecules. *Chem. Phys.* **2008**, *346*, 198–211.

[38] Clabo, D. A.; Allen, W. D.; Remington, R. B.; Yamaguchi, Y.; Schaefer III, H. F. A Systematic Study of Molecular Vibrational Anharmonicity and Vibration–Rotation Interaction by Self-Consistent-Field Higher-Derivative Methods. Asymmetric Top Molecules. *Chem. Phys.* **1998**, *123*, 187–239.

[39] Schneider, W.; Thiel, W. Anharmonic Force Fields from Analytic Second Derivatives: Method and Application to Methyl Bromide. *Chem. Phys. Lett.* **1989**, *157*, 367–373.

[40] Wang, F.; Landau, D. P. Efficient, Multiple-Range Random Walk Algorithm to Calculate the Density of States. *Phys. Rev. Lett.* **2001**, *86*, 2050–2053.

[41] Barone, V. Vibrational Zero-Point Energies and Thermodynamic Functions Beyond the Harmonic Approximation. *J. Chem. Phys.* **2004**, *120*, 3059–3065.

[42] Barone, V. Anharmonic Vibrational Properties by a Fully Automated Second-Order Perturbative Approach. *J. Chem. Phys.* **2005**, *122*, 014108.

[43] Vazquez, J.; Stanton, J. F. Simple(r) Algebraic Equation for Transition Moments of Fundamental Transitions in Vibrational Second-order Perturbation Theory. *Mol. Phys.* **2006**, *104*, 377−388.

[44] Vazquez, J.; Stanton, J. F. Treatment of Fermi Resonance Effects on Transition Moments in Vibrational Perturbation Theory. *Mol. Phys.* **2007**, *105*, 101−109.

[45] Nguyen, T. L.; Barker, J. R. Sums and Densities of Fully Coupled Anharmonic Vibrational States: A Comparison of Three Practical Methods. *J. Phys. Chem.* A **2010**, *114*, 3718–3730.

[46] Bloino, J.; Biczysko, M.; Barone, V. General Perturbative Approach for Spectroscopy, Thermodynamics, and Kinetics: Methodological Background and Benchmark Studies. *J. Chem. Theory Comput.* **2012**, *8*, 1015–1036.

[47] Dzugan, L. C.; Matthews, J.; Sinha, A.; McCoy, A. B. Role of Torsion-Vibration Coupling in the Overtone Spectrum and Vibrationally Mediated Photochemistry of CH_3OOH and HOOH. *J. Phys. Chem. A* **2017**, *121*, 9262–9274.

[48] Pitzer, K. S.; Gwinn, W. D. Energy Levels and Thermodynamic Functions for Molecules with Internal Rotations I. Rigid Frame with Attached Tops. *J. Chem. Phys.* **1942**, *10*, 428–440.

[49] Truhlar, D. G. A Simple Approximation for the Vibrational Partition Function of a Hindered Internal Rotation. *J. Comput. Chem.* **1991**, *12*, 266–270.

[50] Knyazev, V. D.; Dubinsky, I. A.; Slagle, I. R.; Gutman, D. Unimolecular Decomposition of *t*-C_4H_9 Radical. *J. Phys. Chem.* **1994**, *98*, 5279–5289.

[51] Forst, W. Sum and Density of States of Polyatomic Systems with Hindered Rotors. *J. Computational Chem*. **1996**, *17*, 954–961.

[52] McClurg, R. B.; Flagan, R. C.; Goddard III, W. A. The Hindered Rotor Density-of-States Interpolation Function, *J. Chem. Phys.* **1997**, *106*, 6675–6680.

[53] Knyazev, V. D. Density of States of One-Dimensional Hindered Internal Rotors and Separability of Rotational Degrees of Freedom. *J. Phys. Chem. A* **1998**, *102*, 3916–3922.

[54] Ayala, P. Y.; Schlegel, H. B. Identification and Treatment of Internal Rotation in Normal Mode Vibrational Analysis. *J. Chem. Phys.* **1998**, *108*, 2314–2325.

[55] Ellingson, B. A.; Lynch, V. A.; Mielke, S. L.; Truhlar, D. G. Statistical Thermodynamics of Bond Torsional Modes: Tests of Separable, Almost-Separable, and Improved Pitzer–Gwinn Approximations, *J. Chem. Phys.* **2006**, *125*, 084305.

[56] Sharma, S.; Raman, S.; Green, W. H. Intramolecular Hydrogen Migration in Alkylperoxy and Hydroperoxyalkylperoxy Radicals: Accurate Treatment of Hindered Rotors. *J. Phys. Chem. A*, **2010**, *114*, 5689–5701.

[57] Zheng, J.; Yu, T.; Papajak, E.; Alecu, I. M.; Mielke, S. L.; Truhlar, D. G. Practical Methods for Including Torsional Anharmonicity in Thermochemical Calculations on Complex Molecules: The Internal-Coordinate Multi-Structural Approximation. *Phys. Chem. Chem. Phys.* **2011**, *13*, 10885–10907.

[58] Skouteris, D.; Calderini, D.; Barone, V. Methods for Calculating Partition Functions

of Molecules Involving Large Amplitude and/or Anharmonic Motions. *J. Chem. Theory Comput.* **2016**, *12*, 1011–1018.

[59] Li, Y.-P.; Bell, A. T.; Head-Gordon, M. Thermodynamics of Anharmonic Systems: Uncoupled Mode Approximations for Molecules. *J. Chem. Theory Comput.* **2016**, *12*, 2861–2870.

[60] Hsu, K.-H.; Huang, Y.-H.; Lee, Y.-P.; Huang, M.; Miller, T. A.; McCoy, A. B. Manifestations of Torsion-CH Stretch Coupling in the Infrared Spectrum of CH_3OO. J. Phys. Chem. A **2016**, *120*, 4827−4837.

[61] Huang, M.; Miller, T. A.; McCoy, A. B.; Hsu, K.-H.; Huang, Y.-H.; Lee, Y. P. Modeling the CH Stretch/Torsion/Rotation Couplings in Methyl Peroxy (CH_3OO). *J. Phys. Chem. A* **2017**, *121*, 9619–9630.

[62] Ghale, S. B.; Lanorio, J. G.; Nickel, A. A.; Ervin, K. M. Conformational Effects on Gas-Phase Acidities of Isomeric C_3 and C_5 Alkanols. *J. Phys. Chem. A* **2018**, *122*, 7797–7807.

[63] Doll, J. D. Anharmonic Corrections in Unimolecular Theory: A Monte Carlo approach. *Chem. Phys. Lett.* **1980**, *72*, 139–142.

[64] Barker, J. R. Sums of Quantum States for Nonseparable Degrees of Freedom: Multidimensional Monte Carlo Integration. *J. Phys. Chem.* **1987**, *91*, 3849–3854.

[65] M. Berblinger, C. Schlier, J. Tennyson, S. Miller, Accurate Specific Molecular State Densities by Phase Space Integration. II. Comparison with Quantum Calculations on H_3^+ and HD_2^+. *J. Chem. Phys.* **1992**, *96*, 6842–6849.

[66] Berblinger, M.; Schlier. How accurate is the Rice-Ramsperger-Kassel-Marcus theory? The case of H_3^+. *J. Chem. Phys.* **1994**, 101, 4750–4758.

[67] Ming, L.; Nordholm, S.; Schranz, H. W. On the estimation of anharmonic densities of states of molecules, *Chem. Phys. Lett.* **1996**, *248*, 228–236.

[68] Taubmann, G.; Schmatz, S. Numbers and Densities of States and Partition Functions From an Efficient Approach to Phase Space Integration. *Phys. Chem. Chem. Phys.* **2001**, *3*, 2296–2305.

[69] Ma, X.; Yang, N.; Johnson, M. A.; Hase, W. L. Anharmonic Densities of States for Vibrationally Excited $I^-(H_2O)$, $(H_2O)_2$, and $I^-(H_2O)_2$. *J. Chem. Theory Comput.* **2018**, *14*, 3986–3997.

[70] Kamarchik, E.; Jasper, A. W. Anharmonic State Counts and Partition Functions for Molecules via Classical Phase Space Integrals in Curvilinear Coordinates. *J. Chem. Phys.* **2013**, *138*, 194109.

[71] Kamarchik, E.; Jasper, A. W. Anharmonic Vibrational Properties from Intrinsic *n*-Mode State Densities. *J. Phys. Chem. Lett.* **2013**, *4*, 2430–2435.

[72] Whitten, G. Z.; Rabinovitch, B. S. Accurate and Facile Approximation for Vibrational Energy-Level Sums. *J. Chem. Phys*. **1963**, *38*, 2466–2473.

[73] Miller, W. H. Classical Path Approximation for the Boltzmann Density Matrix, *J. Chem. Phys.* **1971**, *55*, 3146–3156.

[74] Messina, M.; Schenter, G. K.; Garrett, B. C. Approximate Path Integral Methods for Partition Functions. *J. Chem. Phys.* **1993**, *98*, 4120–4127.

[75] Wadi, H.; Pollak, E. Accurate Computation of Quantum Densities of States and RRKM Rate Constants for Large Polyatomic Molecules: The STAIR Method. *J. Chem. Phys.* **1999**, *110*, 8246–8253.

[76] Prudente, F. V.; Varandas, A. J. C. A Direct Evaluation of the Partition Function and Thermodynamic Data for Water at High Temperatures. *J. Phys. Chem. A* **2002**, *106*, 6193–6200.

[77] Troe, J.; Ushakov, V. G. Anharmonic Rovibrational Numbers and Densities of States for HO_2, H_2CO, and H_2O_2. *J. Phys. Chem. A* **2009**, *113*, 3940–3945.

[78] Kramer, Z. C; Skodje, R. T. A Semiclassical Adiabatic Calculation of State Densities for Molecules Exhibiting Torsions: Application to Hydrogen Peroxide and its Isotopomers. *Theor. Chem. Acc.* **2014**, *133*, 1530.

[79] Jasper, A. W.; Gruey, Z. B.; Harding, L. B.; Georgievski, Y.; Klippenstein, S. J.; Wagner, A. F. Anharmonic Rovibrational Partition Functions for Fluxional Species at High Temperatures via Monte Carlo Phase Space Integrals. *J. Phys. Chem. A* **2018**, *122*, 1727–1740.

[80] Feynman, R. P.; Hibbs, A. R. *Quantum Mechanics and Path Integrals*; McGraw-Hill: New York, 1965.

[81] Ceperly, D. M. Path Integrals in the Theory of Condensed Helium. *Rev. Mod. Phys.* **1995**, *67*, 279–355.

[82] Leonard, C.; Handy, N. C.; Carter, S.; Bowman, J. M. The Vibrational Levels of Ammonia. *Spectrochim. Acta, Part A* **2002**, *58*, 825–838.

[83] Braams, B. J.; Bowman, J. M. Permutationally Invariant Potential Energy Surfaces in High Dimensionality. *Int. Rev. Phys. Chem*. **2009**, *28*, 577–606.

[84] Špirko, V.; Jensen, P.; Bunker, P. R.; Čejchan, A. The Development of a New Morse-Oscillator Based Rotation–Vibration Hamiltonian for H_3^+. *J. Molec. Spectroscopy* **1985**, *112*, 183–202.

[85] Isaacson, A. D.; Truhlar, D. G. The Accuracy of the Pitzer-Gwinn Method for Partition Functions of Anharmonic Vibrational Modes. *J. Chem. Phys.* **1981**, *75*, 4090–4094.

[86] Lynch, V. A.; Meilke, S. L.; Truhlar, D. G. Accurate Vibrational-Rotational Partition Functions and Standard-State Free Energy Values for H_2O_2 from Monte Carlo Path-Integral Calculations. *J. Chem. Phys.* **2004**, *121*, 5148–5162.

[87] Bross, D. H.; Jasper, A. W.; Ruscic, B.; Wagner, A. F. Toward Accurate High Temperature Anharmonic Partition Functions. *Proc. Combust. Inst.* **2019**, *37*, 315–322.

[88] NIST Computational Chemistry Comparison and Benchmark Database NIST Standard Reference Database Number 101, Release 19, April 2018, Editor: Russell D. Johnson III. http://cccbdb.nist.gov/ DOI:10.18434/T47C7Z

[89] Harding, L. B.; Klippenstein, S. J.; Jasper, A. W. Ab Initio Methods for Reactive Potential Energy Surfaces. *Phys. Chem. Chem. Phys.* **2007**, *9*, 4055–4070.

[90] Jasper, A. W.; Hansen, N. Hydrogen-Assisted Isomerizations of Fulvene to Benzene and of Larger Cyclic Aromatic Hydrocarbons. *Proc. Combust. Inst.* **2013**, *34*, 279–287.

[91] Klippenstein, S. J. From Theoretical Reaction Dynamics to Chemical Modeling of Combustion. *Proc. Comb. Inst*. **2017**, *36*, 77–111.

[92] Fernandez-Ramos, A.; Ellingson, B. A.; Garrett, B. C.; Truhlar, D. G. "Variational Transition State Theory with Multidimensional Tunneling," in *Reviews in Computational Chemistry*, Vol. 23, Lipkowitz, K. B.; Cundari, T. R., eds. (Wiley-VCH; Hoboken, NJ, 2007), pp. 125–232.

[93] Jasper, A. W.; Pelzer, K. M.; Miller, J. A.; Kamarchik, E.; Harding, L. B.; Klippenstein, S. J. Predictive A Priori Pressure-Dependent Kinetics. *Science* **2014**, *346*, 1212–1215.

[94] Klippenstein, S. J.; Harding, L. B.; Ruscic, B. Ab Initio Computations and Active Thermochemical Tables Hand in Hand: Heats of Formation of Core Combustion Species. *J. Phys. Chem. A* **2017**, *121*, 6580–6602.

Figure Captions

Fig. 1. Average rovibrational anharmonicity corrections per-mode for five nonfluxional species. The average of the five results is shown as a sold black line and labeled (0,0).

Fig. 2. Average rovibrational anharmonicity corrections per-mode for four species with one inversion. In (a) results for all rotational and vibrational modes are shown. In (b) the inversion is described using a one-dimensional (1D) model, and Γ for the remaining nonfluxional modes are shown. The average of the results in each panel is shown as a sold blue line and labeled (0,1), with the reference (0,0) result included for comparison. In (b) black circles show the result of correcting for anharmonic coupling to overall rotation for CH_2.

Fig. 3. Average rovibrational anharmonicity corrections per-mode for nine species with one torsion. In (a) results for all rotational and vibrational modes are shown. In (b) the inversion is described using a one-dimensional (1D) model, and Γ for the remaining nonfluxional modes are shown. In (c) the 1D model has been corrected by the projection correction factor $\hat{f}$. The average of the results in each panel is shown as a sold blue line and labeled (1,0), with the reference (0,0) result included for comparison.

Fig. 4. Average rovibrational anharmonicity corrections per-mode for four species with one torsion and one inversion. In (a) results for all rotational and vibrational modes are shown, and in (b) the torsion and inversion are described using the projected reduced-dimensional 2D model, and results for the remaining nonfluxional modes are shown. In (c) the torsion and inversion are described using the projected 2x1D model. The average of the results in each panel is shown as a sold blue line and labeled (1,1), with the reference (0,0) result included for comparison.

Fig. 5. Two-dimensional cuts through the potential energy surfaces for the four (1,1) systems. Critical point energies are shown in cm^{-1} relative to the minimum-energy well, and the number of apostrophes indicates the order of the saddle point.

Fig. 6. Average rovibrational anharmonicity corrections per-mode for four species with

two torsions. In (a) results for all rotational and vibrational modes are shown, and in (b) the torsions are described using the projected reduced-dimensional 2D model, and results for the remaining nonfluxional modes are shown. In (c) the torsions are described by the projected 2x1D model. The average of the results in each panel is shown as a sold blue line and labeled (2,0), with the reference (0,0) result included for comparison.

Fig. 7. Two-dimensional cut through the potential energy surface for acetone. Critical point energies are shown in cm^{-1} relative to the minimum-energy well, and the number of apostrophes indicates the order of the saddle point.

Fig. 8. Two-dimensional cuts through the potential energy surfaces for four (2,0) systems. Critical point energies are shown in cm^{-1} relative to the minimum-energy well, and the number of apostrophes indicates the order of the saddle point.

Fig. 9. Two-dimensional cuts through the potential energy surfaces for two (2,0) systems. Critical point energies are shown in cm^{-1} relative to the minimum-energy well, and the number of apostrophes indicates the order of the saddle point.

Fig. 10. Average rovibrational anharmonicity corrections per-mode for four species with torsions and inversions. In (a) results for all rotational and vibrational modes are shown, and in (b) the fluxional modes are described using the projected reduced-dimensional 3D model, and results for the remaining nonfluxional modes are shown. In (c) the fluxional modes are described by the projected 3x1D model. The average of the results in each panel is shown as a sold blue line and labeled (2,1),(1,2), with the reference (0,0) result included for comparison.

Fig. 11. Two-dimensional cuts through the potential energy surfaces for two (2,0) systems. Critical point energies are shown in cm^{-1} relative to the minimum-energy well, and the number of apostrophes indicates the order of the saddle point.

Fig. 12. Two-dimensional cuts through the potential energy surface for CH_3CHOH. Critical point energies are shown in cm^{-1} relative to the minimum-energy well,

and the number of apostrophes indicates the order of the saddle point.

Fig. 13. Average rovibrational anharmonicity corrections per-mode for four species with three torsions. In (a) results for all rotational and vibrational modes are shown, and in (b) the torsions modes are described using the projected reduced-dimensional 3D model, and results for the remaining nonfluxional modes are shown. In (c) the torsions are described by the projected 3x1D model. The average of the results in each panel is shown as a sold blue line and labeled (3,0), with the reference (0,0) result included for comparison.

Fig. 14. Two-dimensional cuts through the potential energy surface for CH_3OOCH_3. Critical point energies are shown in cm^{-1} relative to the minimum-energy well, and the number of apostrophes indicates the order of the saddle point.

Fig. 15. Two-dimensional cut through the potential energy surface for $CH(OH)_3$. Critical point energies are shown in cm^{-1} relative to the minimum-energy well, and the number of apostrophes indicates the order of the saddle point.

Fig. 16. Two-dimensional cuts through the potential energy surface for $HOCH_2CH_2OH$. Critical point energies are shown in cm^{-1} relative to the minimum-energy well, and the number of apostrophes indicates the order of the saddle point.

Figure 1

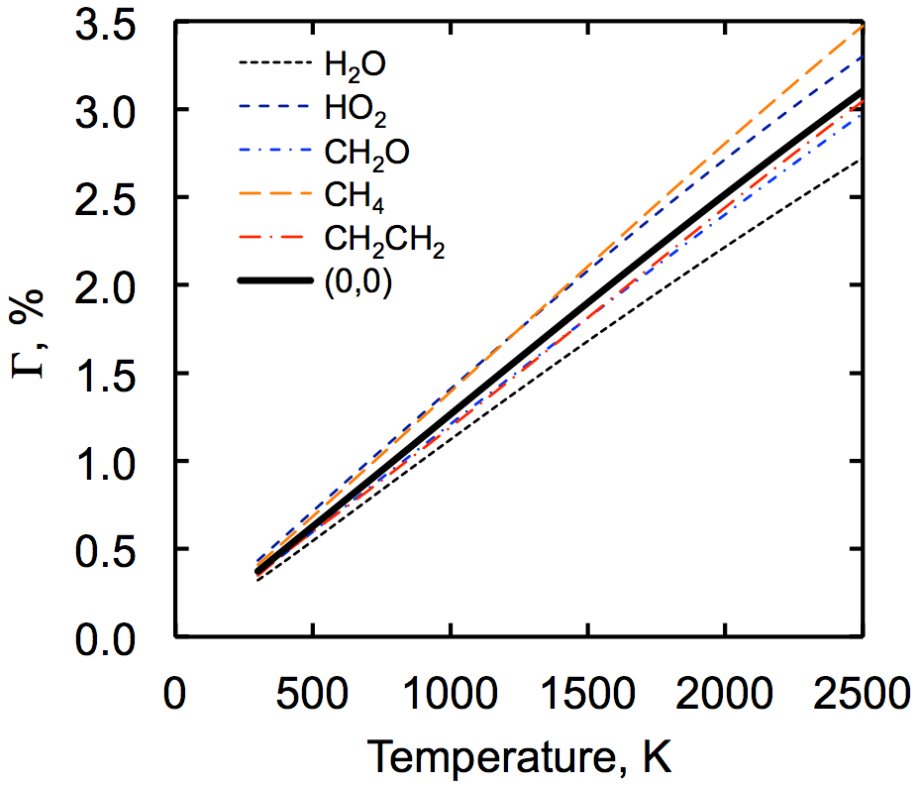

Fig. 1. Average rovibrational anharmonicity corrections per-mode for five nonfluxional species. The average of the five results is shown as a sold black line and labeled (0,0).

Figure 2

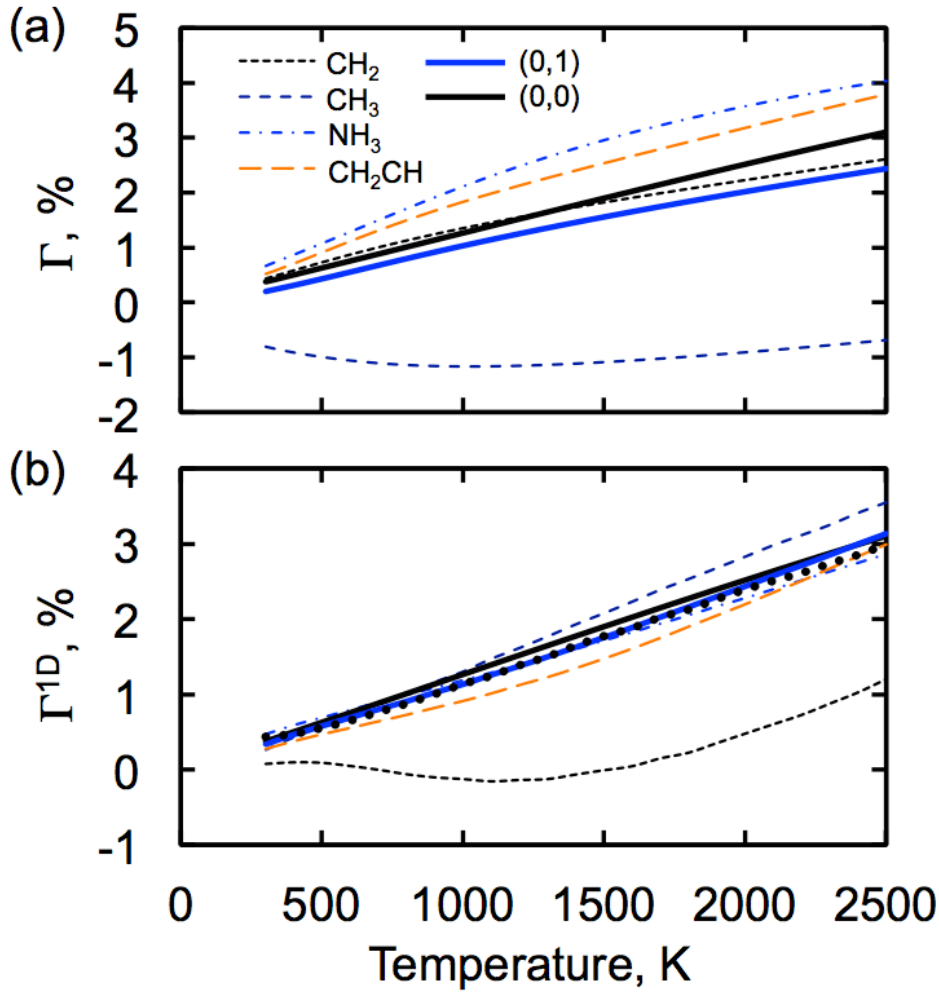

Fig. 2. Average rovibrational anharmonicity corrections per-mode for four species with one inversion. In (a) results for all rotational and vibrational modes are shown. In (b) the inversion is described using a one-dimensional (1D) model, and Γ for the remaining nonfluxional modes are shown. The average of the results in each panel is shown as a sold blue line and labeled (0,1), with the reference (0,0) result included for comparison. In (b) black circles show the result of correcting for anharmonic coupling to overall rotation for CH_2.

Figure 3

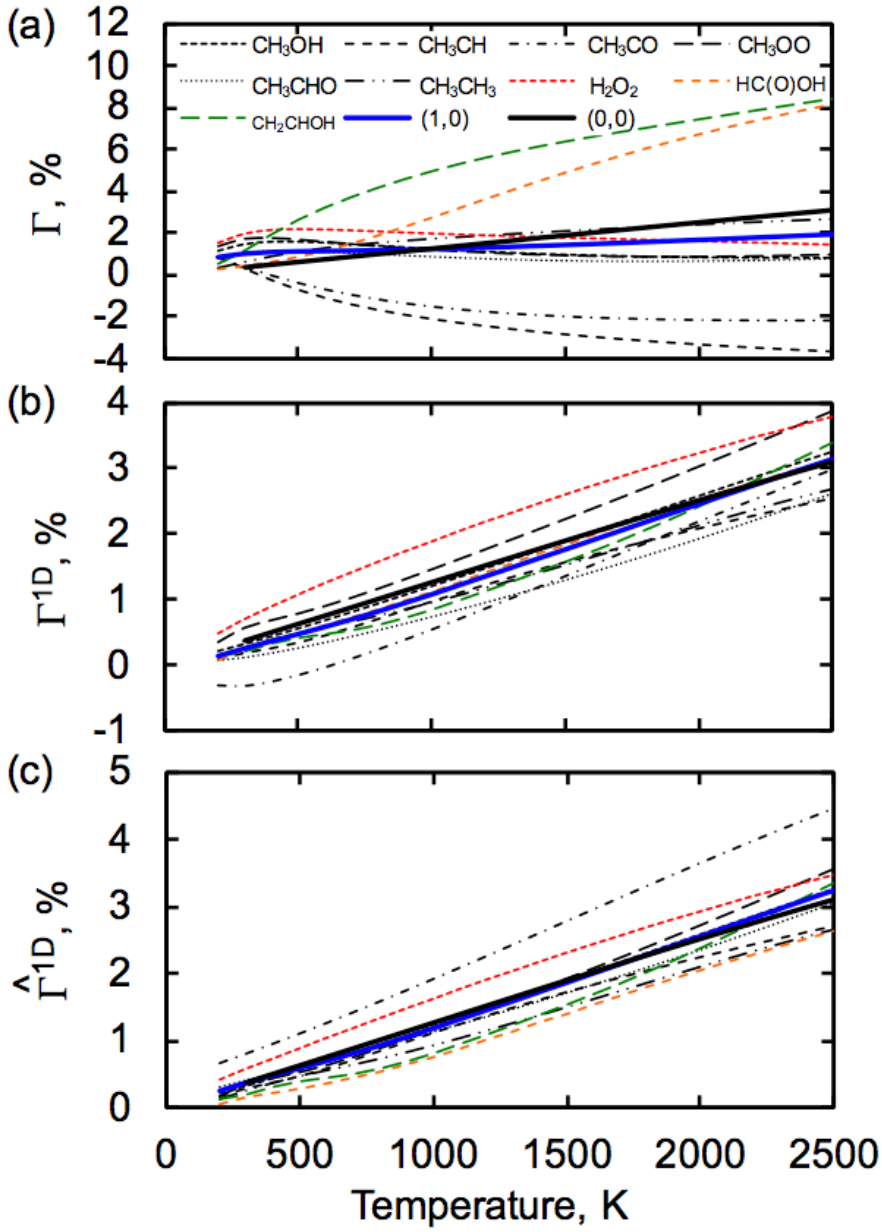

Fig. 3. Average rovibrational anharmonicity corrections per-mode for nine species with one torsion. In (a) results for all rotational and vibrational modes are shown. In (b) the inversion is described using a one-dimensional (1D) model, and Γ for the remaining nonfluxional modes are shown. In (c) the 1D model has been corrected by the projection correction factor $\hat{f}$. The average of the results in each panel is shown as a sold blue line and labeled (1,0), with the reference (0,0) result included for comparison.

Figure 4

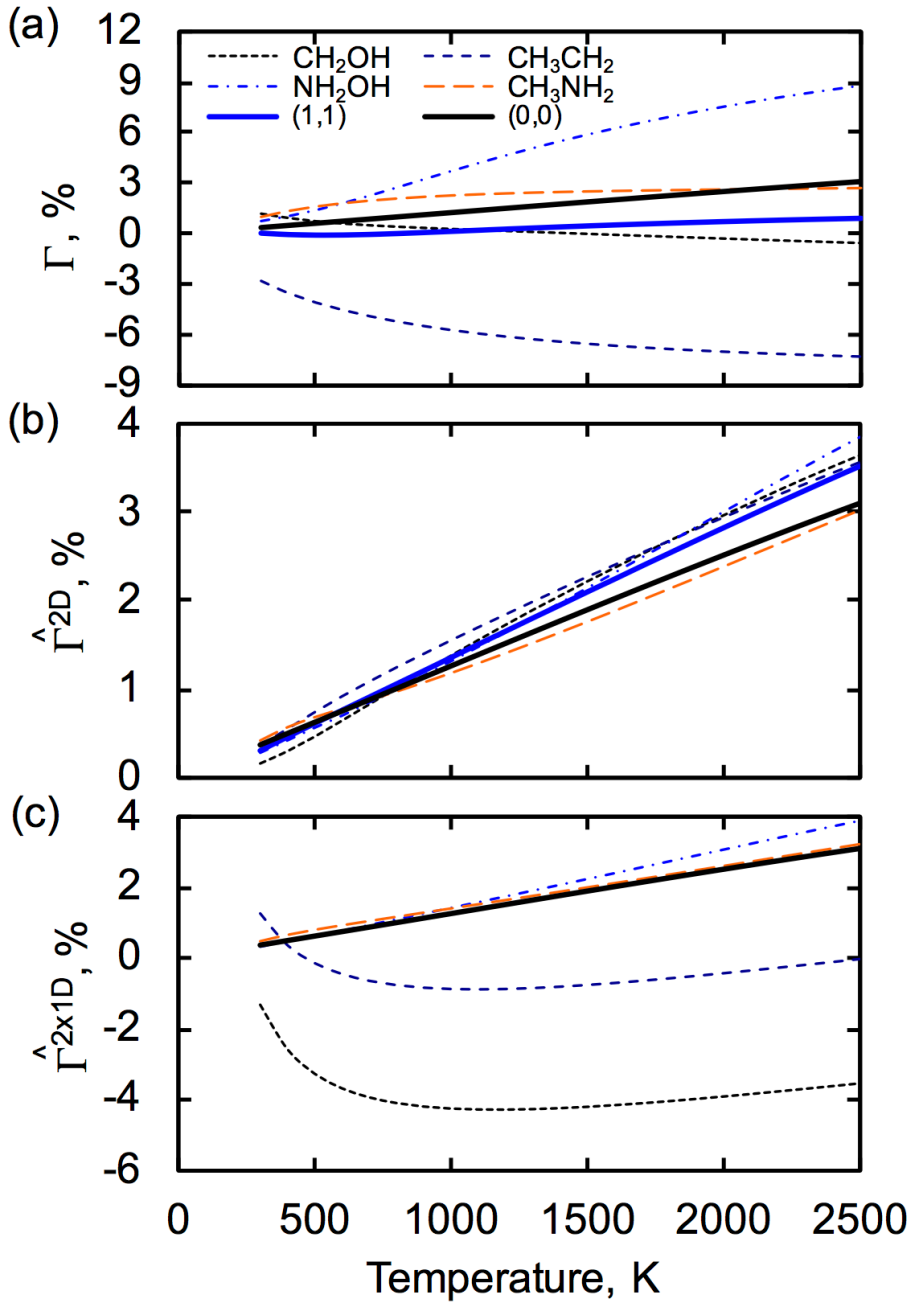

Fig. 4. Average rovibrational anharmonicity corrections per-mode for four species with one torsion and one inversion. In (a) results for all rotational and vibrational modes are shown, and in (b) the torsion and inversion are described using the projected reduced-dimensional 2D model, and results for the remaining nonfluxional modes are shown. In (c) the torsion and inversion are described using the projected 2x1D model. The average of the results in each panel is shown as a sold blue line and labeled (1,1), with the reference (0,0) result included for comparison.

Figure 5

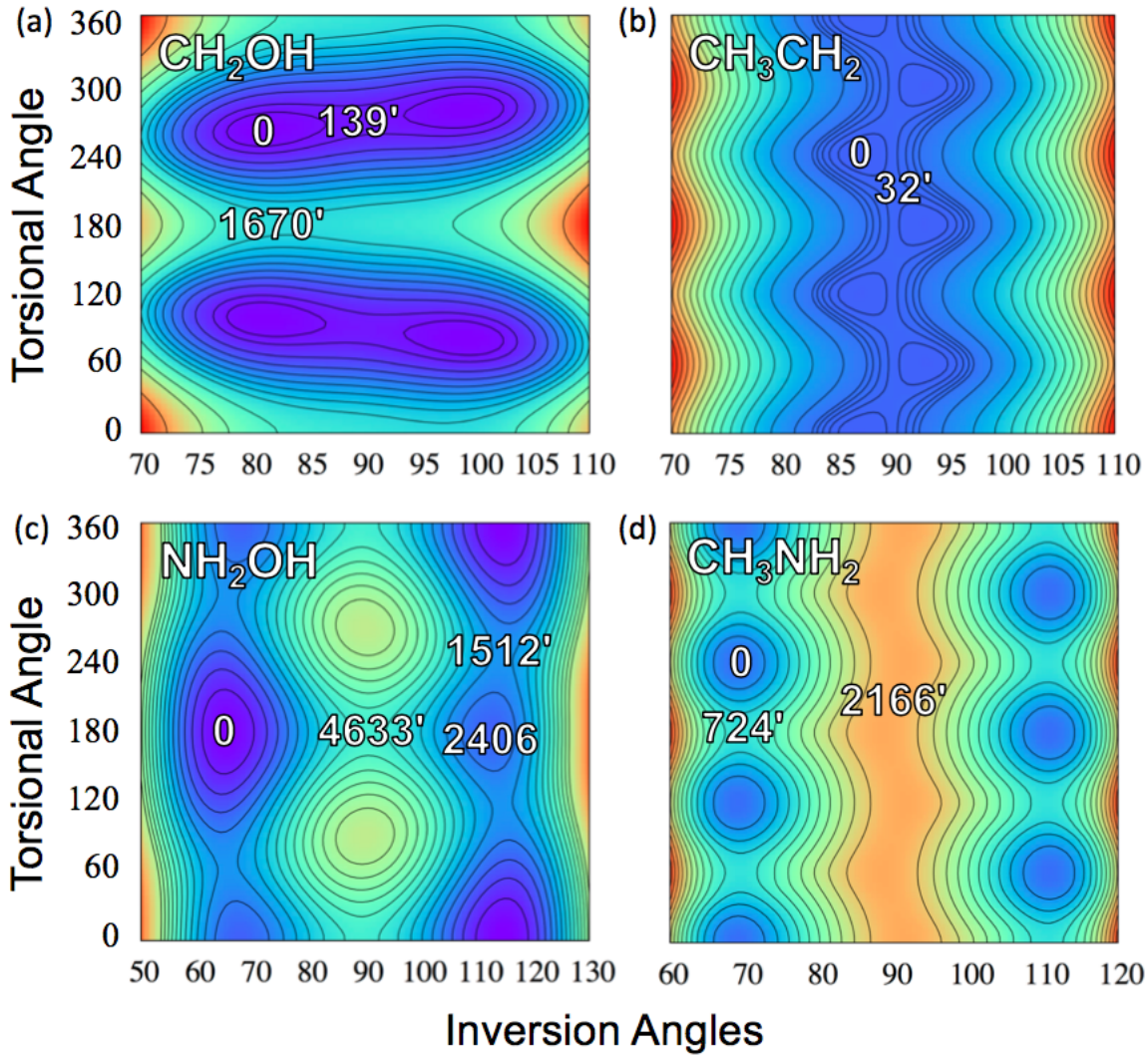

Fig. 5. Two-dimensional cuts through the potential energy surfaces for the four (1,1) systems. Critical point energies are shown in cm^{-1} relative to the minimum-energy well, and the number of apostrophes indicates the order of the saddle point.

Figure 6

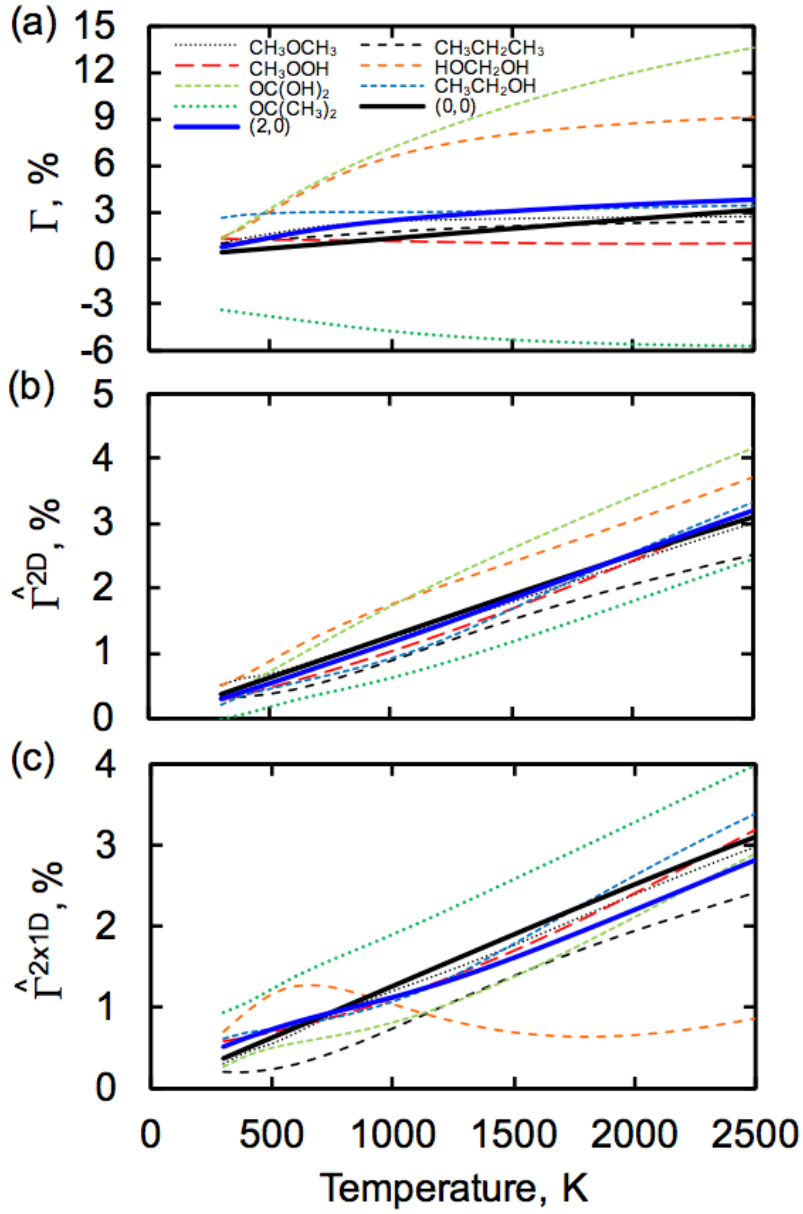

Fig. 6. Average rovibrational anharmonicity corrections per-mode for four species with two torsions. In (a) results for all rotational and vibrational modes are shown, and in (b) the torsions are described using the projected reduced-dimensional 2D model, and results for the remaining nonfluxional modes are shown. In (c) the torsions are described by the projected 2x1D model. The average of the results in each panel is shown as a sold blue line and labeled (2,0), with the reference (0,0) result included for comparison.

Figure 7

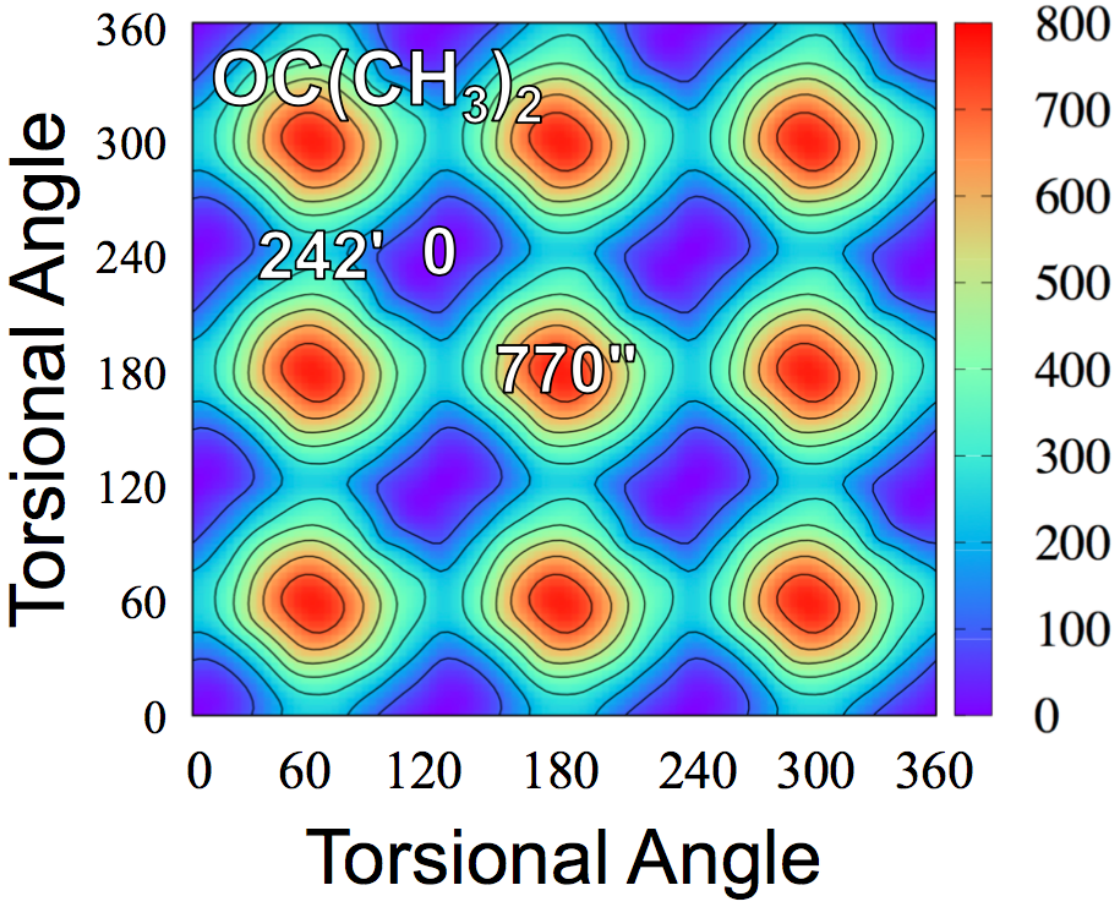

Fig. 7. Two-dimensional cut through the potential energy surface for acetone. Critical point energies are shown in cm^{-1} relative to the minimum-energy well, and the number of apostrophes indicates the order of the saddle point.

Figure 8

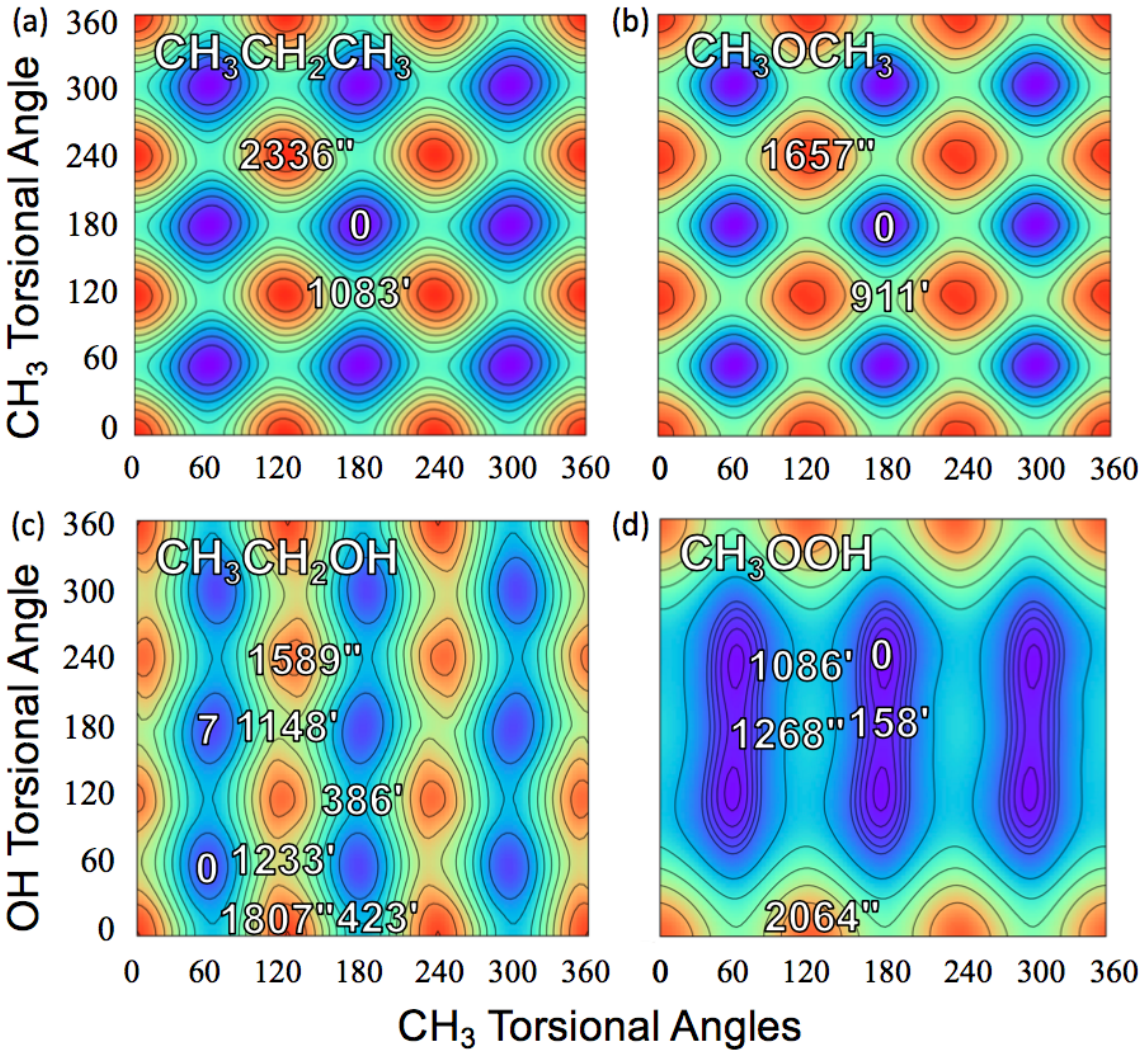

Fig. 8. Two-dimensional cuts through the potential energy surfaces for four (2,0) systems. Critical point energies are shown in cm^{-1} relative to the minimum-energy well, and the number of apostrophes indicates the order of the saddle point.

Figure 9

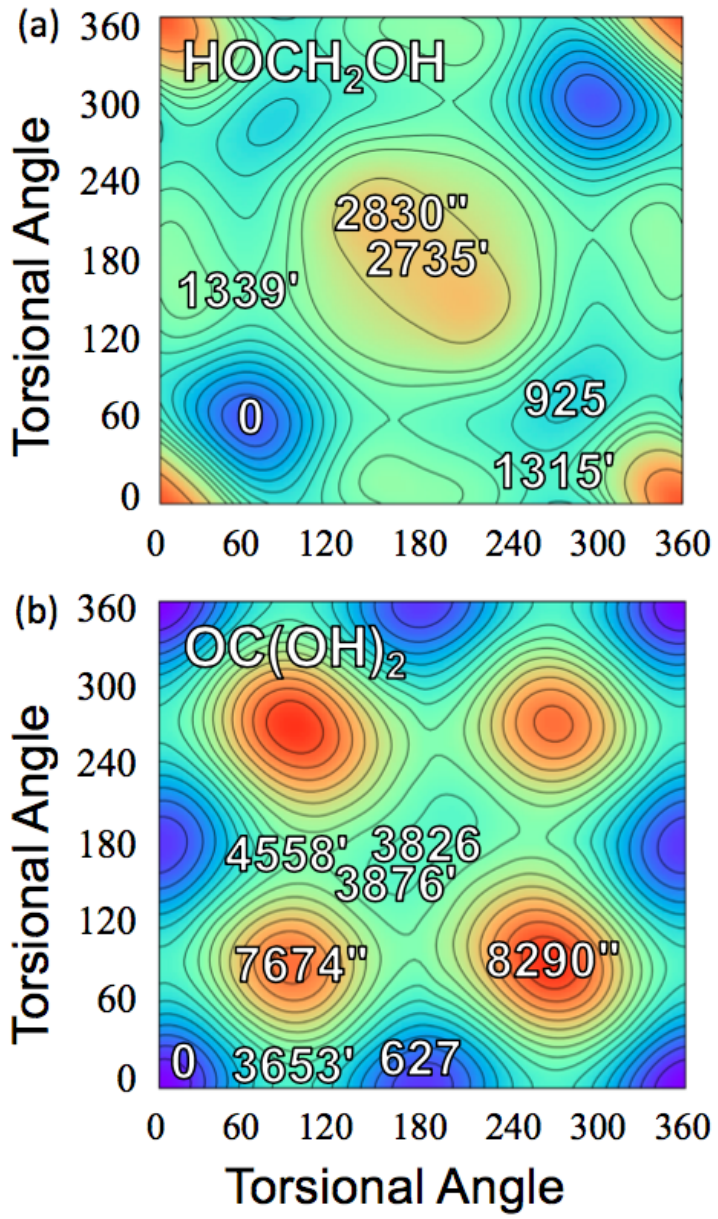

Fig. 9. Two-dimensional cuts through the potential energy surfaces for two (2,0) systems. Critical point energies are shown in cm^{-1} relative to the minimum-energy well, and the number of apostrophes indicates the order of the saddle point.

Figure 10

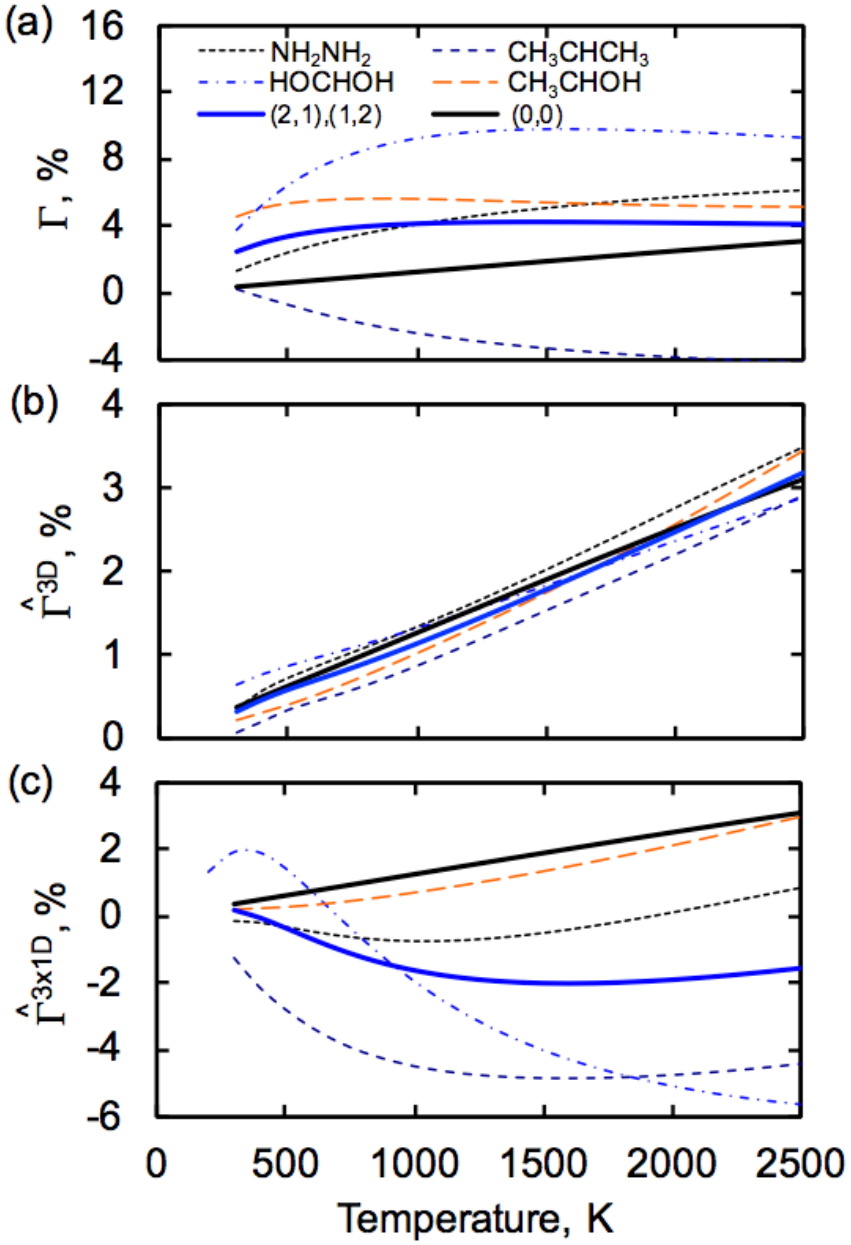

Fig. 10. Average rovibrational anharmonicity corrections per-mode for four species with torsions and inversions. In (a) results for all rotational and vibrational modes are shown, and in (b) the fluxional modes are described using the projected reduced-dimensional 3D model, and results for the remaining nonfluxional modes are shown. In (c) the fluxional modes are described by the projected 3x1D model. The average of the results in each panel is shown as a sold blue line and labeled (2,1),(1,2), with the reference (0,0) result included for comparison.

Figure 11

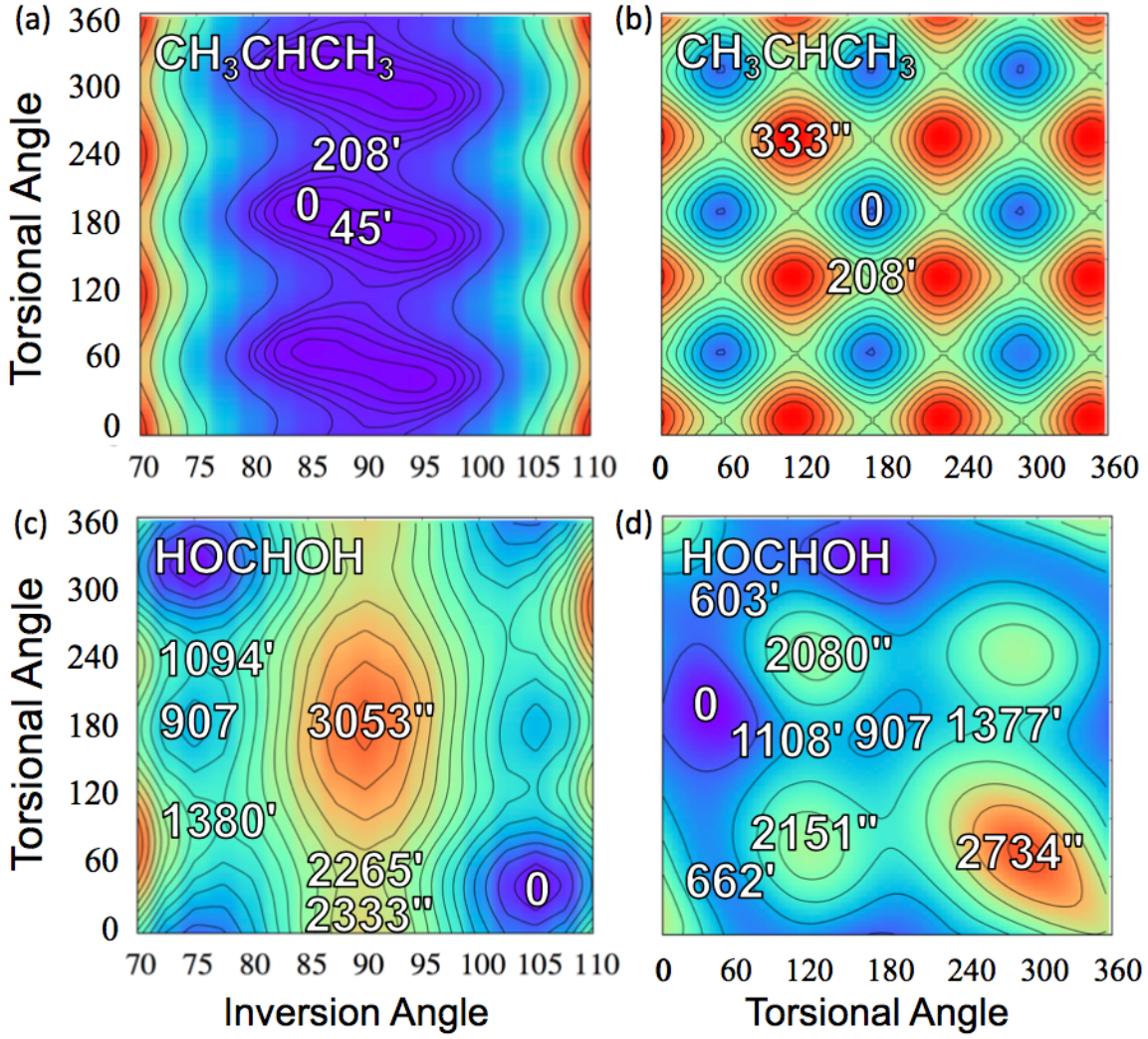

Fig. 11. Two-dimensional cuts through the potential energy surfaces for two (2,0) systems. Critical point energies are shown in cm^{-1} relative to the minimum-energy well, and the number of apostrophes indicates the order of the saddle point.

Figure 12

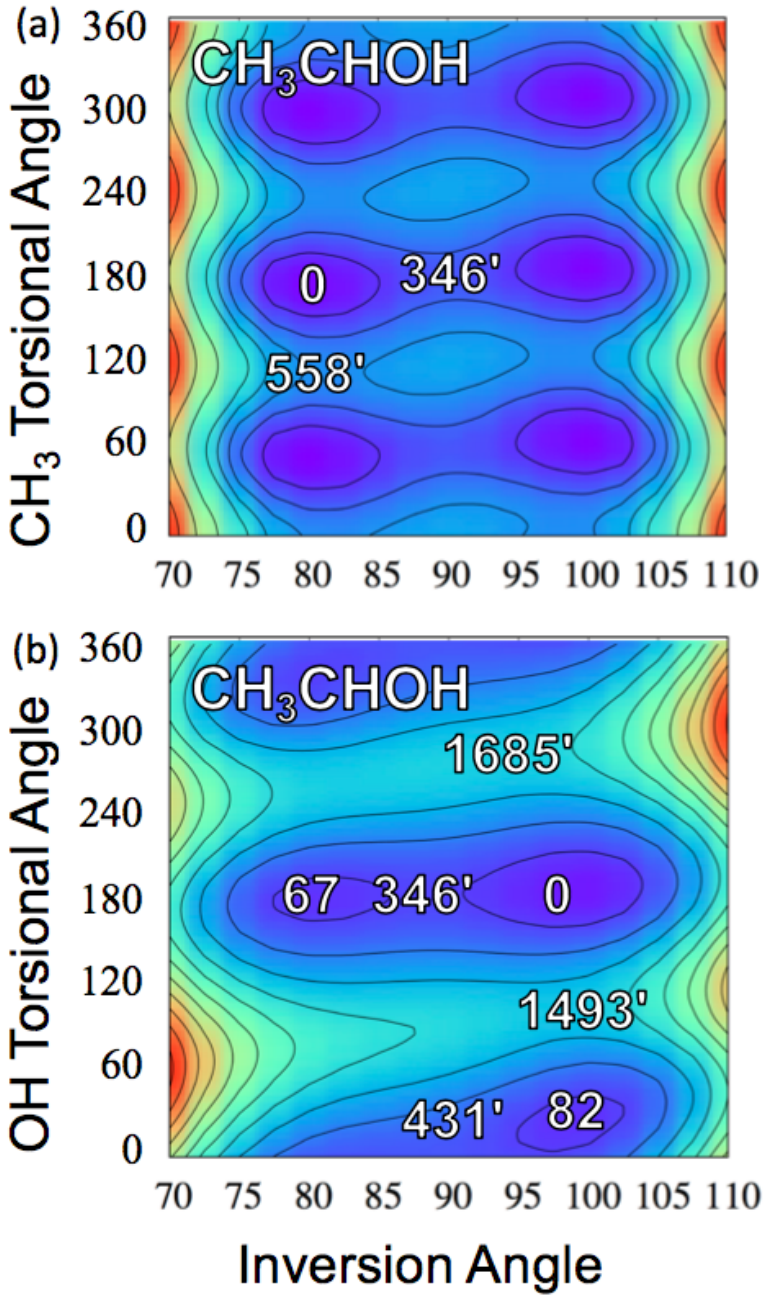

Fig. 12. Two-dimensional cuts through the potential energy surface for CH_3CHOH. Critical point energies are shown in cm^{-1} relative to the minimum-energy well, and the number of apostrophes indicates the order of the saddle point.

Figure 13

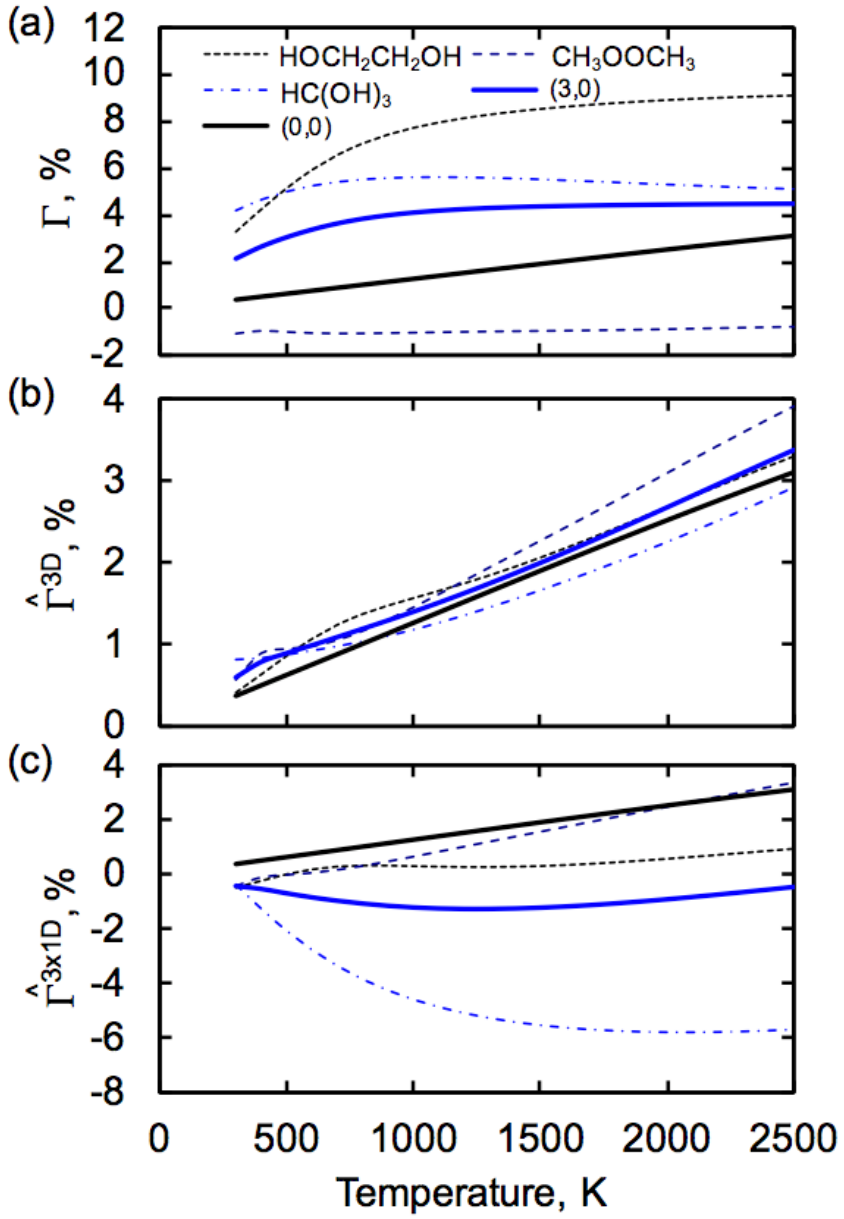

Fig. 13. Average rovibrational anharmonicity corrections per-mode for four species with three torsions. In (a) results for all rotational and vibrational modes are shown, and in (b) the torsions modes are described using the projected reduced-dimensional 3D model, and results for the remaining nonfluxional modes are shown. In (c) the torsions are described by the projected 3x1D model. The average of the results in each panel is shown as a sold blue line and labeled (3,0), with the reference (0,0) result included for comparison.

Figure 14

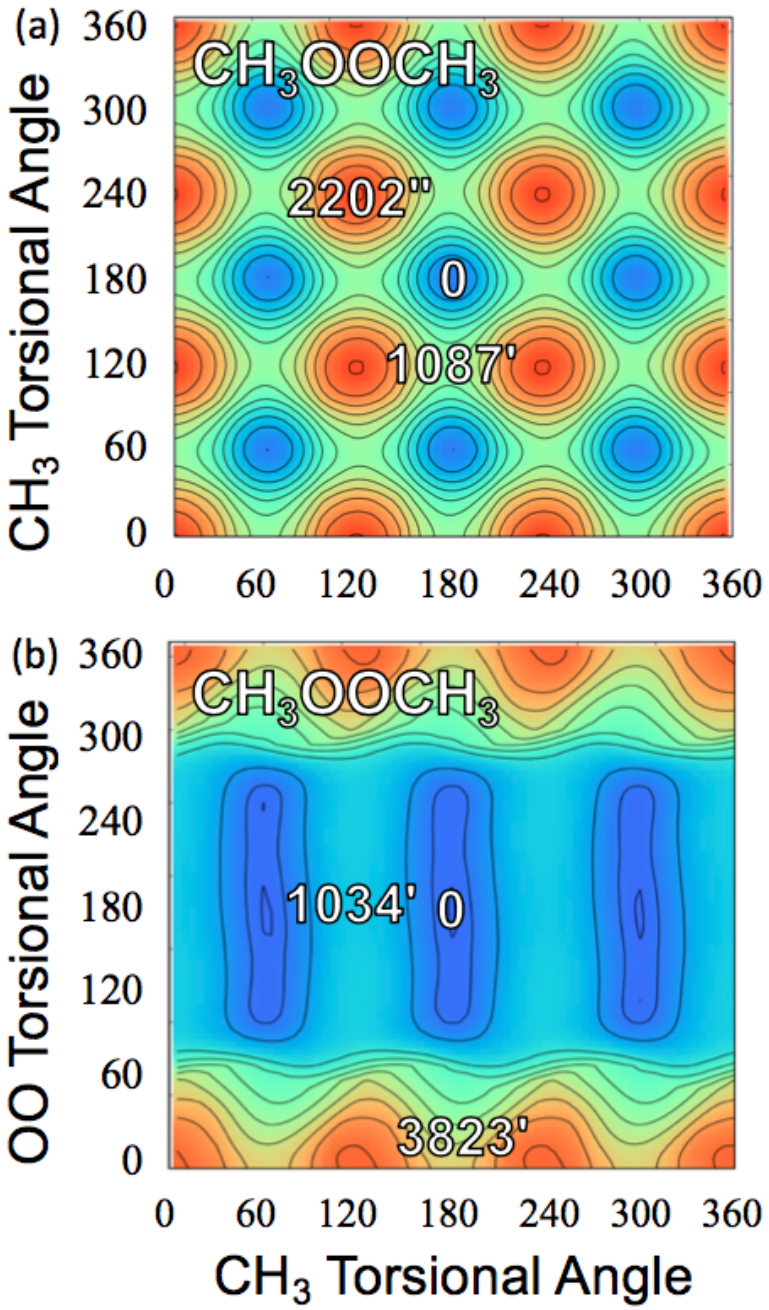

Fig. 14. Two-dimensional cuts through the potential energy surface for CH_3OOCH_3. Critical point energies are shown in cm^{-1} relative to the minimum-energy well, and the number of apostrophes indicates the order of the saddle point.

Figure 15

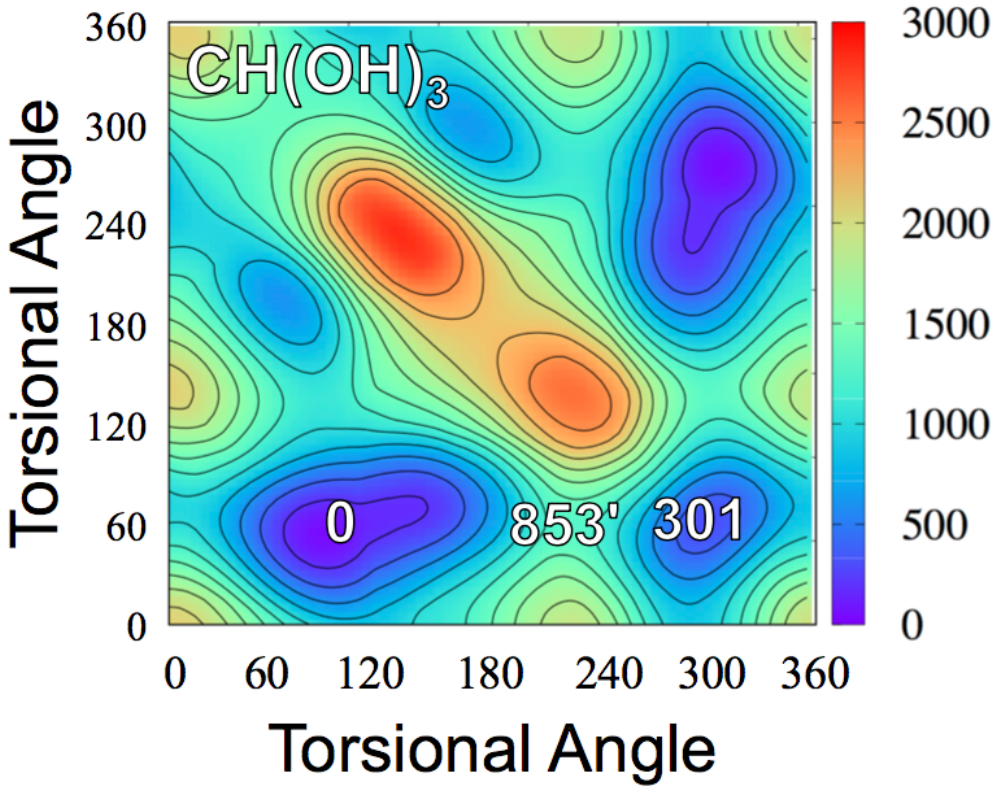

Fig. 15. Two-dimensional cut through the potential energy surface for $CH(OH)_3$. Critical point energies are shown in cm^{-1} relative to the minimum-energy well, and the number of apostrophes indicates the order of the saddle point.

Figure 16

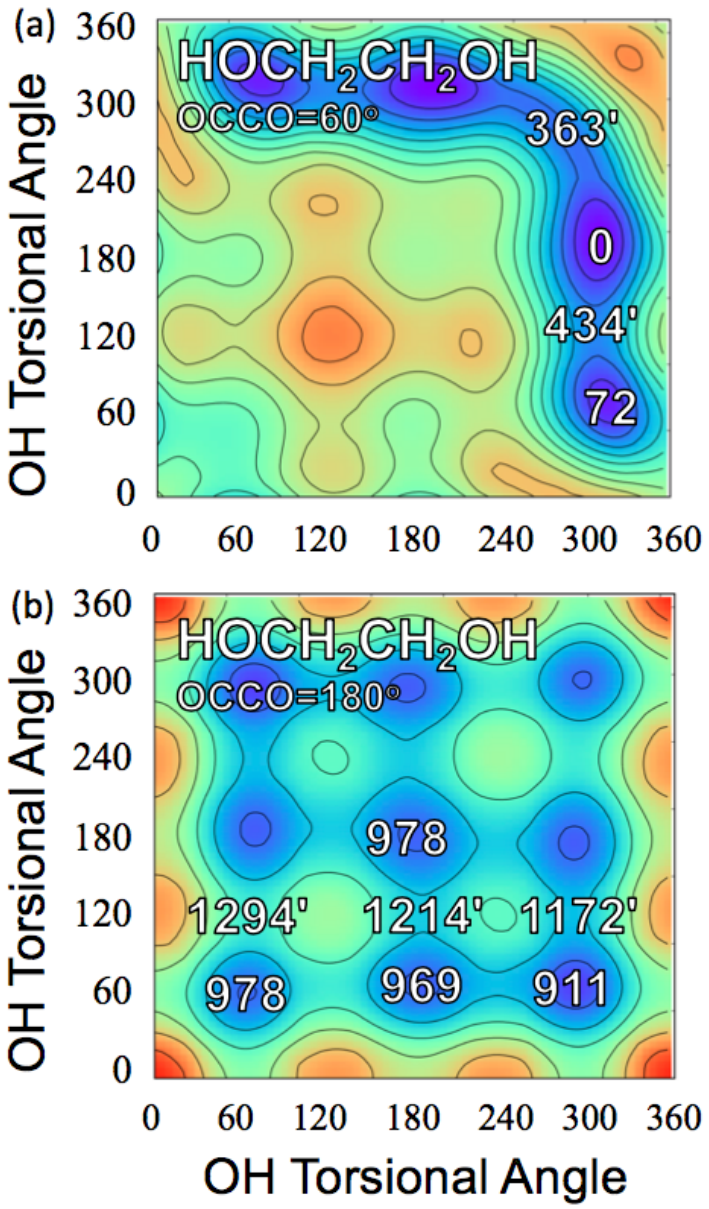

Fig. 16. Two-dimensional cuts through the potential energy surface for $HOCH_2CH_2OH$. Critical point energies are shown in cm^{-1} relative to the minimum-energy well, and the number of apostrophes indicates the order of the saddle point.

TOC Graphic

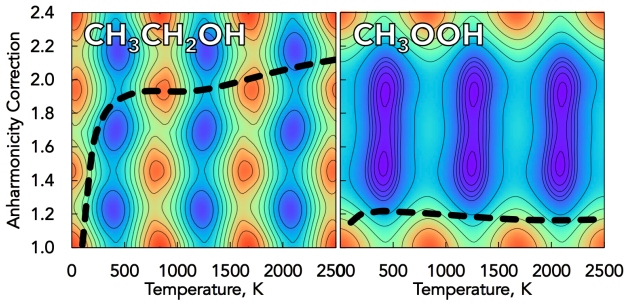
CH3CH2OH
CH3OOH
Anharmonicity Correction
2.4
2.2
2.0
1.8
1.6
1.4
1.2
1.0
0
500
1000
1500
2000
2500
Temperature, K
Temperature, K